Generating a Stable Higher-Symmetry $CsPbI_3$ Perovskite Phase in Ambient Conditions: Unveiling the Stabilization Mechanism

Rafikul Ali Saha[1*], Athina Papadopoulou[2,3], Rocío Ariza[1], Giedrius Degutis[2], Irina Skvortsova[4], Tom Braeckevelt[5,6], Francesco De Angelis[7], Eduardo Solano[8], João Pedro de Sousa Gouveia dos Anjos[2,9], Maria Isabel Pintor Monroy[2], Ilya Mongilyov[10], Bart Goderis[10], Juan Rubio-Zuazo[11,12], Jan Genoe[2,3], Carlo Meneghini[7], Julian A. Steele[13,14], Sara Bals[4], Veronique Van Speybroeck[5], Johan Hofkens[6,15], Maarten B. J. Roeffaers[1*]

[1] *cMACS, Department of Microbial and Molecular systems, KU Leuven, Celestijnenlaan 200F, Heverlee, 3001 Belgium*

[2] *imec, Kapeldreef 75, 3001 Leuven, Belgium*

[3] *Department of Electrical Engineering (ESAT), KU Leuven, Kasteelpark Arenberg 10, 3001 Leuven, Belgium*

[4] *Electron Microscopy for Materials Science(EMAT) and NANOlab Center of Excellence, University of Antwerp, B-2020 Antwerp, Belgium*

[5] *Center for Molecular Modeling (CMM),Ghent University, Technologiepark 46, 9052 Zwijnaarde, Belgium;*

[6] *Department of Chemistry, KU Leuven, Celestijnenlaan 200F, Leuven 3001, Belgium*

[7] *Department of Science, Roma Tre University, via Della Vasca Navale 84, 00146 Rome, Italy*

[8] *NCD-SWEET beamline, ALBA synchrotron light source, 08290, Cerdanyola del Vallès, Barcelona, Spain*

[9] *i3N/CENIMAT, Department of Materials Science, Faculty of Science and Technology, Universidade NOVA de Lisboa and CEMOP/UNINOVA, Campus de Caparica, 2829-516 Caparica, Portugal*

[10] *Polymer Chemistry and Materials, Department of Chemistry, KU Leuven, Celestijnenlaan 200F, Heverlee, 3001 Belgium*

[11] *BM25-SpLine Beamline at the ESRF,71 Avenue des Martyrs, Grenoble, 38043, France*

[12] *Instituto de Ciencia de Materiales de Madrid-CSIC, Sor Juana Inés de la Cruz, 3, Cantoblanco, 28049 Madrid, Spain*

[13] *Australian Institute for Bioengineering and Nanotechnology (AIBN), The University of Queensland, Brisbane, QLD, 4072, Australia*

[14]*School of Mathematics and Physics, The University of Queensland, Brisbane, QLD, 4072, Australia*

[15]*Department of Molecular Spectroscopy, Max Planck Institute for Polymer Research, Mainz 55128, Germany*

(*) rafikulali.saha@kuleuven.be, maarten.roeffaers@kuleuven.be

Keywords: Dimethylammonium Iodide, Higher symmetry black phase, Strain, Octahedral tilting, Photodetector

Abstract: The black-phase cesium lead iodide ($CsPbI_3$) is a promising candidate for high-efficiency perovskite optoelectronics, but its instability under ambient conditions remains a major challenge. Among several strategies, dimethylammonium iodide (DMAI) has emerged as a potential stabilizer; however, inconsistencies in phase stability (3–7 days) and lower solar power conversion efficiencies (~20% vs. ~27% for hybrid perovskites) highlight the need for further improvements. This study not only demonstrates enhanced stabilization of the high-symmetry black phase of $CsPbI_3$ and improved film morphology through optimized composition and annealing conditions, but more importantly provides detailed mechanistic insights obtained from comprehensive experimental and theoretical analysis. Systematic tuning of DMAI concentration (1.2 M), annealing temperature (200°C, 1 min), and Cs^+ substitution (12–15%) significantly extends phase stability to 7 days under ambient conditions (35–52% relative humidity) and maintains stability even after 16 months in a dry-box environment by reducing orthorhombic strain and octahedral tilting. Additionally, a minor (~5%) 0D Cs_4PbI_6 phase fills pinholes, enhancing film quality. Optimized photodiodes exhibit low dark current (~1 $\mu A/cm^2$), high external quantum efficiency (~80% at -2 V), and a ≥100 dB linear dynamic range. These findings provide mechanistic insights into the stabilization of the black phase of $CsPbI_3$, advancing the development of more stable and efficient perovskite-based optoelectronic devices.

Introduction

Inorganic metal halide perovskites, specifically $CsPbI_3$, have attracted tremendous attention as highly promising material for photovoltaic (PV) and photodetector (PD) applications due to their chemical stability, high temperature sustainability (~370 °C), cost-effective solution-processability, and rapidly increasing conversion efficiencies[1–5]. Despite its remarkable performance, its real-world application faces limitations in two crucial areas. The initial concern pertains to its phase stability[6–9], while the subsequent issue revolves around effectively addressing defects within thin films[10–13]. The photoactive black phase polymorphs (perovskite phase) of $CsPbI_3$ (α, β, and γ) with a bandgap of ~1.7 eV, remain stable only at elevated temperatures. At room temperature (RT), it transforms into a yellow, nonperovskite photoinactive phase (δ) with a bandgap of 2.82 eV[6–9,14,15]. While the black phase might persist for a short duration when cooled to RT, it eventually reverts to the yellow phase after a few minutes, particularly in the presence of oxygen and moisture[6]. Since both PV and PD devices operate on similar principles of light absorption and electron excitation, and effective PV materials are also highly suitable for PDs, stabilizing the photoactive black phase of $CsPbI_3$ under ambient conditions is essential for enhancing performance in both applications.

Several strategies have been developed to improve the stability of black-$CsPbI_3$ as well as its PV performance. The most promising approaches include: (i) creating 0D/3D heterostructures, which result in approximately 2 days of stability and a power conversion efficiency (PCE) of around 14-16%[16–18]; (ii) substituting I with Br (forming $CsPbI_2Br$), which achieves 16-21% PCE with several hours stability[19–22]; and (iii) incorporating dimethylammonium iodide (DMAI) during $CsPbI_3$ synthesis, achieving approximately 20% PCE with 3-7 days stability[23–29]. Among these approaches, the use of DMAI has recently gained attention for its ability to significantly enhance both stability and solar cell performance[17,30,31]. However, its full potential remains limited due to an incomplete understanding of its stabilization mechanisms. However, their stability varies significantly, ranging from 3 to 7 days. Furthermore, their PCE, approximately 20%, still lags behind that of organic-inorganic hybrid counterparts, which achieve PCEs of 27% or higher in perovskite solar cells[32–34]. The underlying reasons for the variability in stability and lower PCE are not yet fully understood.

Moreover, there is a significant ongoing debate regarding the role of DMAI in stabilization and PV performance of $CsPbI_3$. While some researchers state that DMA^+ might replace Cs^+[25,26,28], others propose that DMAI acts as an additive rather than a substitution[24]. According to Wang *et al.*[24], DMAI acts as an additive, not an organic cation dopant, playing a role in stabilizing β-$CsPbI_3$ at room temperature, but the residue of DMAI deteriorate both stability and PV performance. In contrast, Meng *et al.*[26] and Eperon *et al.*[25] advocate that DMA^+ substituting Cs^+ and this tactic yields samples with stable, resulting in notable PCE of ~20% [25,26,35]. Additionally, Liu *et al.*[27] propose utilizing DMAI to form γ-$DMA_xCs_{1-x}PbI_3$, Cs_4PbI_6, and δ-$DMA_xCs_{1-x}PbI_3$, with the composition of these phases adjustable by varying the annealing dwell time. These differences in observed behavior could be governed by key synthesis parameters such as DMAI concentration, annealing temperature, and dwelling time at peak temperature. However, to further elevate black phase stability and PCE, it remains highly important to comprehensively uncover the impact of DMAI throughout the entire process. Numerous pressing questions remain unanswered, including the nature of the generated phases, the potential alloying of DMA ions within the perovskite structure, and the factors (DMAI concentration, annealing temperature, and dwelling time at peak temperature) catalyzing the crystallization of the $CsPbI_3$ perovskite phase and morphology at RT. Acquiring a comprehensive understanding of this strategy and addressing the aforementioned inquiries would empower us to finely manipulate the composition and quality of $CsPbI_3$ films. This, in turn, holds the promise of further enhancing the black phase stability and performance of $CsPbI_3$ devices.

To address the aforementioned questions, we here systematically investigated DMAI-doped $CsPbI_3$ films, their morphology, electronic and atomic structure, the relationship between structure and phase transition temperature, and the stability of the black phase under various annealing temperatures and dwelling times. This investigation has been carried out through a multiphysics approach using complementary techniques to study the crystallization processes of the DMAI-based method, with a focus on adjusting the ratios of DMAI: PbI_2:CsI in the precursor solution and varying the annealing duration. Our analysis has demonstrated that 12-15% of Cs^+ is replaced by DMA^+, leading to a notable reduction in orthorhombic strain and an enhancement of octahedral Pb-I-Pb bond angle. This has implied a transition towards a higher symmetric phase at RT, resulting in a significantly more stable black phase with stability increase of 700 times compared to DMAI-absent $CsPbI_3$. Our optimized thin film remained remarkably stable, showing no changes even after 16 months in a dry box environment. The black phase underwent a stabilization period of seven days under full air exposure, with a relative humidity ranging from 35% to 52%. Throughout the synthesis process, the transformation of $DMAPbI_3$ occurred into both the 0D Cs_4PbI_6 and 3D $CsPbI_3$ phases (see Materials and Methods section for reaction mechanism). This 0D phase tended to form at pinhole locations, effectively filling these areas and improving the morphology of the thin film while reducing defect states. Finally, we demonstrated the mechanism underlying the enhanced black-phase stability and photodetector performance in the optimized thin film, achieved through precise control of annealing temperature and dwell time.

Result and Discussion

Unveiling the thermal-phase relationship: structural dynamics and impact of DMAI.

To investigate the influence of DMAI on the phase behavior of $CsPbI_3$ thin films, we conducted a comprehensive comparative analysis of two materials: $CsPbI_3$ (without DMAI) and DMAI-$CsPbI_3$ (with DMAI), focusing on their structural, morphological, and stability characteristics.

We fabricated thin films of $CsPbI_3$ and DMAI-$CsPbI_3$ using spin coating (synthesis procedures are detailed in the Materials and Methods section). To investigate the influence of DMAI, we employed three different molar ratios of DMAI:PbI_2:CsI, specifically 0.5:1:1, 1.2:1:1, and 1.5:1:1 (chemical reactions are illustrated in the Materials and Methods section). Based on the black-phase stability time, we determined an optimized molar ratio of 1.2:1:1 for the present study (Explained in the Materials and Methods section and Figure 1 and S1).

Initially, at RT, both thin films ($CsPbI_3$ and DMAI-$CsPbI_3$) appeared yellow (see Figure 1A). For $CsPbI_3$ thin films, the yellow thin film transformed to black at 350 °C (annealing under N_2), as shown in Figure 1A. During the quenching to RT under N_2, it retained its black color; however, upon exposure to air (ambient conditions), it reverted to yellow within a few minutes (see the top panel of Figure 1A). Conversely, for DMAI-$CsPbI_3$ thin films, two distinct scenarios were observed, as represented in Figure 1A. First, the RT yellow thin film transformed into black at 200 °C, but reverted to yellow after approximately 5-6 minutes at 200 °C or upon further temperature increase. This yellow film once again turned black at 350 °C and remained black after cooling to RT under N_2. However, exposure to ambient conditions caused the black film to revert to yellow similar as the undoped film (see Figure 1A). The second scenario encompassed annealing the thin film under N_2 up to 200 °C, causing the RT yellow color to transition into black. Subsequently, the film is cooled down to RT under N_2. Remarkably, in this scenario, the black film maintained its stability for several days, even following exposure to ambient air.

With a focus on assessing the stability of the RT black phase under ambient conditions, we tracked the conversion time from black to yellow phase using a Leica microscope (see Materials and Methods section). To observe the kinetics of this conversion, we employed the Johnson-Mehl-Avrami-Kolmogorov (JMAK) equation $Y = 1 - e^{-K(t-t_0)n}$, which describes the fraction of transformed perovskite (Y) over time (t)[36], dependent on exponent K (the rate of degradation kinetics) , and *n* which is related to the dimensionality of the new nucleating phase. For both $CsPbI_3$ and DMAI-$CsPbI_3$ samples, when achieving the RT black phase after cooling down from 350 °C under N_2, this black phase exhibited rapid conversion to the yellow phase within a short span (10-15 minutes) upon exposure to air (K = 0.0024 min^{-1}, and 0.0022 min^{-1}, respectively), as shown in Figure 1B. Notably, in the case of DMAI-$CsPbI_3$, the stability of the black phase after cooling from 200 °C depended on the dwelling time at 200 °C (see Figure S2). A dwelling time of approximately 1 minute resulted in significantly extended stability, lasting for up to ~10400 min (7 days) ($K = 2.42\times10^{-12}$ min^{-1}) , as shown in Figure 1C). In all instances, consistent *n* values (n = 3) were obtained, indicating that the degradation process was uniform and independent of the annealing temperature. These findings suggest a clear influence of annealing temperature and dwelling time on the black to yellow phase degradation kinetic rates.

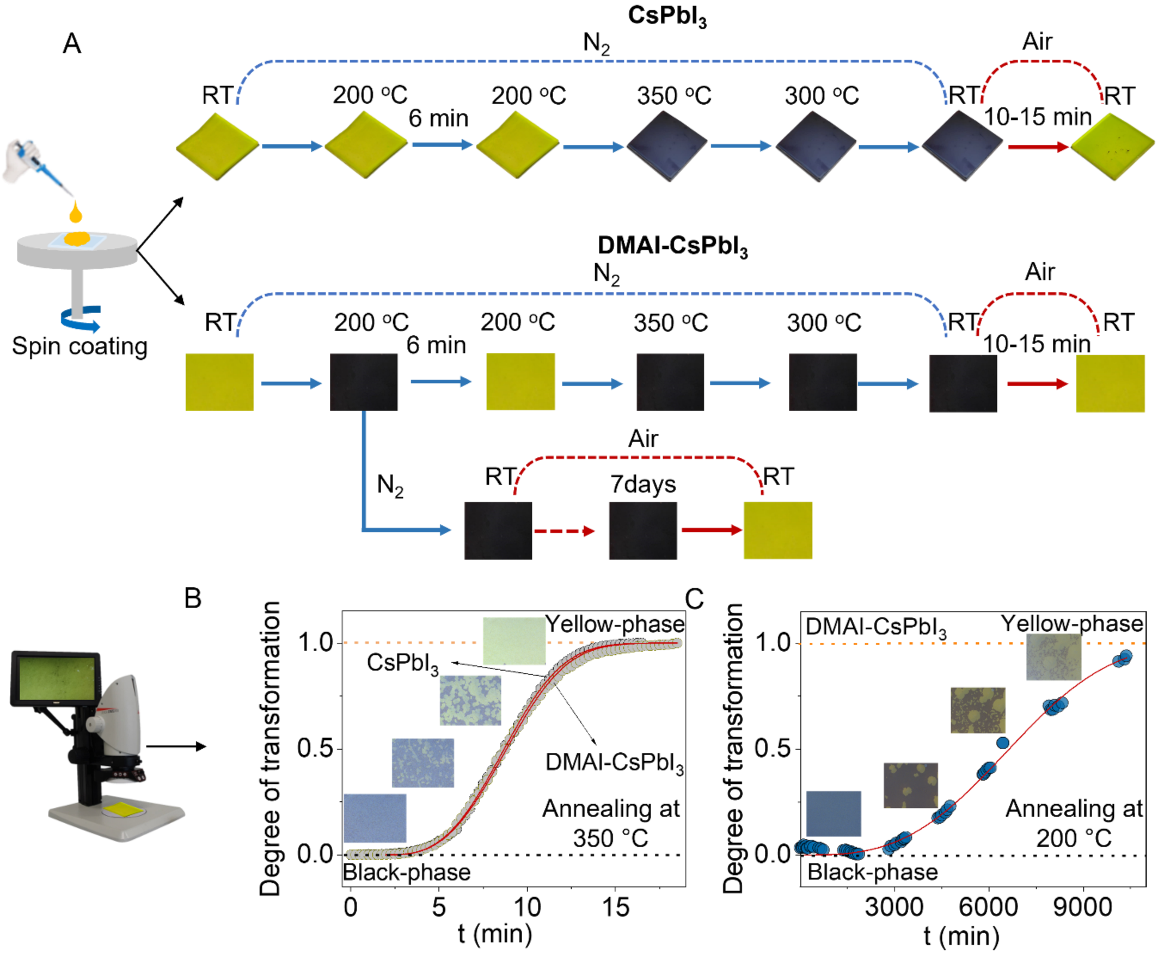

Figure 1. (A) Temperature-dependent color change observed in two thin films: $CsPbI_3$ (top panel) and DMAI-$CsPbI_3$ (bottom panel), captured using a camera. (B) Degree of phase transformation from black phase to yellow phase at RT for $CsPbI_3$ and DMAI-$CsPbI_3$ after annealing at 350 °C. (C) Degree of phase transformation from black phase to yellow phase at RT for DMAI-$CsPbI_3$ after annealing at 200 °C

It was important to understand the evolution of crystallographic phases during the thermal treatments, and to gain this insights, we conducted temperature-dependent Grazing-Incidence Wide-Angle X-ray Scattering (GIWAXS) measurements under N_2 environment on both $CsPbI_3$ and DMAI-$CsPbI_3$ thin films, as depicted in Figures 2A–C. By employing Rietveld refinement of the GIWAXS data, we identified the crystal structures of the materials and correlated them with the observed film color changes (all crystal structure parameters are provided in Table S1 and S2). In the case of $CsPbI_3$, the yellow-colored sample at RT corresponded to the pure delta phase (δ), and at 350 °C, it converted into the alpha phase (α). During the cooling cycle, the α-phase transformed into the beta phase (β) at around 300 °C, and at RT, the black-colored thin film represented the pure gamma phase (γ) (The 2D GIWAXS image and Rietveld refinement of the azimuthally integrated GIWAXS data, along with the corresponding crystal structure parameters, are shown in Figures S3 and S4, and Table S1). Upon exposure to air, the γ-phase reverted to the δ-phase within a few minutes. For DMAI-$CsPbI_3$, the yellow-colored film at RT included a mixture of $DMAPbI_3$ (Hexagonal space group: P63/mmc; phase fraction: 75%) and Cs_4PbI_6 (Trigonal space group: R-3c; phase fraction: 25%) (The 2D GIWAXS image and Rietveld refinement of the azimuthally integrated GIWAXS data, along with the corresponding crystal structure parameters, are shown in Figures S5 and S6, and Table S2). Annealing at 200 °C induced the black color, which primarily linked to the β-phase of $CsPbI_3$ (95%) along with a minor amount of Cs_4PbI_6 (5%), and cooling the black DMAI-$CsPbI_3$ thin film from 200 °C (β-phase + Cs_4PbI_6) to RT, resulted in an RT phase corresponding to the perovskite-phase (95%) and Cs_4PbI_6 (5%) (see Figure S5 and S6, and Table S2). Interestingly, the room temperature perovskite phase of DMAI-$CsPbI_3$ obtained by cooling from 200 °C (designated as γ*) is significantly different from the typical RT γ-phase of $CsPbI_3$ obtained by cooling from 350 °C, (see Figure S7 and S8A). The DMAI-$CsPbI_3$ sample cooled from 200 °C exhibits a noticeable shift in the perovskite Bragg peaks toward lower q (or 2θ) values compared to the pure $CsPbI_3$ sample cooled from 350 °C (as shown in Figure S8A). This shift strongly suggests that the larger DMA^+ cation (ionic radius: 2.72 Å) has substituted for Cs^+ (ionic radius: 1.88 Å) within the perovskite lattice. The GIWAXS analysis of the room temperature black phase of DMAI-$CsPbI_3$ revealed approximately 12-15% Cs^+ is replaced by DMA^+. Such substitution increases the Goldschmidt tolerance factor[37] $t = \frac{r_A + r_X}{\sqrt{2}(r_B + r_X)}$; ($r_A$, r_B, and r_X are ionic radius of A-, B-, and X-site ion, respectively) which has been widely correlated with an increase in structural symmetry[38], as shown in Figure S8B. Additionally, Rietveld refinement of the GIWAXS data enabled extraction of lattice parameters and atomic positions, allowing reconstruction of the full crystal structures (see Table S1 and S2) and revealing an increase in the average Pb-I-Pb bond angle from 152° in $CsPbI_3$ to 158° in DMAI-$CsPbI_3$ (See Figure S9). Therefore, the RT phase of DMAI-$CsPbI_3$ (obtained by cooling from 200 °C) exhibited higher symmetry compared to the conventional γ-phase of $CsPbI_3$, yet it was less symmetrical than the β-phase of $CsPbI_3$, designated as γ* (see Figure S7 and 2D). The distinction between the γ and γ* phases was further elucidated using x-ray absorption spectroscopy, as detailed in section 2.2. However, this γ*-phase demonstrated remarkable stability, retaining its black color for an extended period (~7 days) even after air exposure. With further cooling, additional diffraction peaks emerged, transitioning into the conventional γ-phase at -80 °C, as depicted in Figure S10.

Alternatively, monitoring DMAI-$CsPbI_3$ thin film at 200 °C for a few minutes (5-6 min) or increasing the temperature caused the mixture of β-phase and Cs_4PbI_6 to transform into the pure δ-phase of $CsPbI_3$. Upon further heating to 350 °C, the δ-phase shifts to the pure α-phase of $CsPbI_3$ (see Figure S11 and S12). Upon quenching from 350 °C to RT, the material exhibited behavior similar to pure $CsPbI_3$ without DMAI doping. In the case of DMAI-$CsPbI_3$ cooled from 200 °C, a small amount of residual DMAI remains, which can lead to the formation of mixed-cation $DMA_xCs_{1-x}PbI_3$ phases. This disrupts the CsI/PbI_2 stoichiometric balance and promotes the formation of the Cs_4PbI_6 phase. In contrast, annealing at a higher temperature (around 350 °C) enables complete evaporation of DMAI, resulting in a phase-pure $CsPbI_3$ film (see Figure S7). These observations enabled the establishment of a thermal phase relationship for $CsPbI_3$ and DMAI-$CsPbI_3$, as illustrated in Figure 2D.

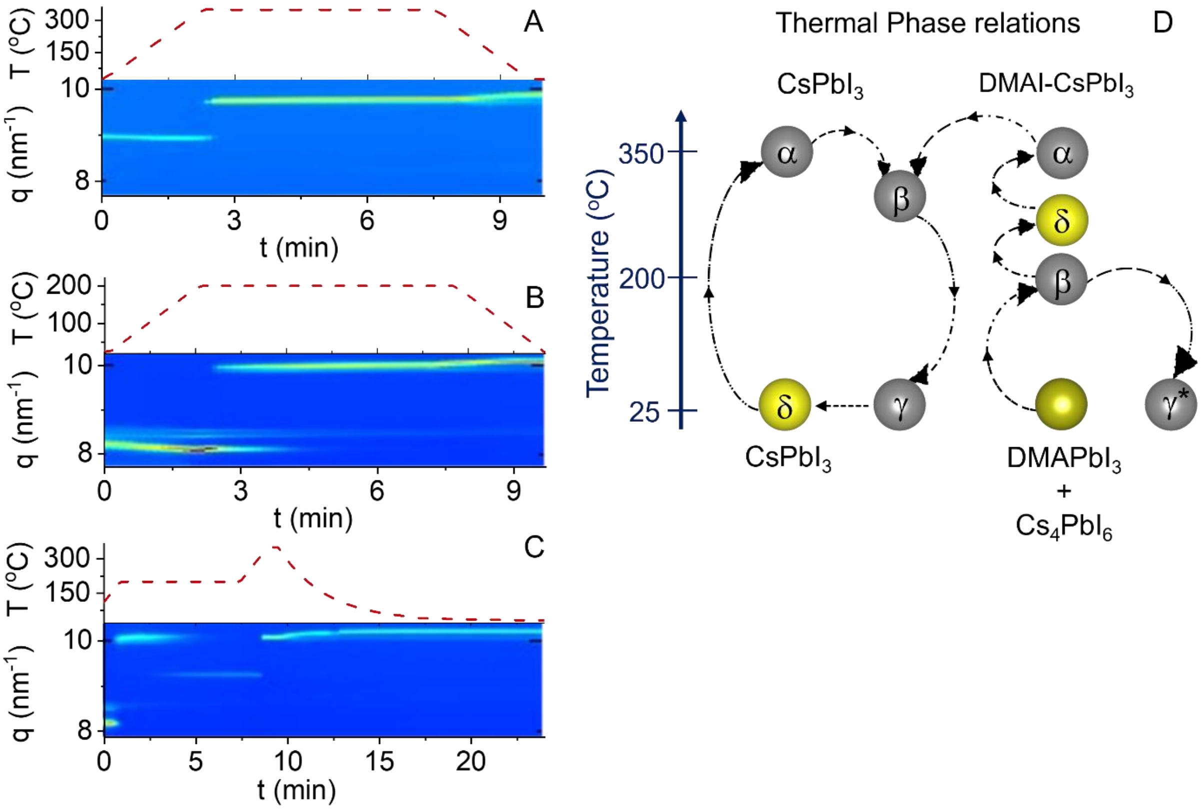

Figure 2. *In situ* GIWAXS t–T profile $(q_{x,y,z})$ through high-temperature yellow-to-black phase transition, followed by thermal cycling under different atmospheres. (A) $CsPbI_3$ without DMAI, (B-C) DMAI-$CsPbI_3$ thin films. (D) Thermal-phase relations of $CsPbI_3$ thin films without and with DMAI.

Differentiation of γ and γ* phases in DMAI-$CsPbI_3$ using local structure probe.

Crystallographic analysis can accurately describe the crystallographic structure in the samples, but it is not sensitive to aperiodic features such as grain boundaries, impurities, disorder (chemical or structural) that can affect the thin film structure at the atomic level. X-ray absorption spectroscopy, as a chemically selective, local probe, is particularly well suited to gain a deeper understanding of these features. Therefore, we investigated the effect of DMAI treatment on the local structure around Pb in $CsPbI_3$ and DMAI-$CsPbI_3$ thin films using Pb L_3-edge X-ray absorption fine structure (XAFS) analysis. XAFS measurements were performed at RT on pure and DMAI-$CsPbI_3$ thin films before and after annealing at 200 °C (conducted *in situ* to prevent air exposure) under a helium atmosphere (inert conditions). Experimental details and data analysis are provided in the Materials and Methods section.

The near edge (XANES) features of the absorption spectra are very sensitive to small variations in valence state, chemistry and local coordination geometry around the absorber[39]. Notably, the position and shape of the Pb-L_3 edge remained consistent across $CsPbI_3$ and DMAI-$CsPbI_3$ thin films, regardless of composition or thermal treatment. This indicates that the Pb valence state, coordination chemistry, and coordination symmetry were largely unaffected by DMAI doping (see Figure S13A).

The XAFS features above the edge (Figure S13A) are sensitive to the modifications of the local atomic structure (interatomic distances and disorder) around the absorber atom and the differences highlighted in the inset of Figure S13A indicate structural modifications of the Pb local structure with respect to the pristine $CsPbI_3$ film. In the k-weighted extended (EXAFS) region (Figure S13B) these changes are even more evident. The k-weighted Pb EXAFS data of all the samples were quantitatively analyzed fitting the experimental spectra to the theoretical model using a multi-shell data refinement to access next neighbour shells details (see Materials and Methods section), representative best fits on $CsPbI_3$ and DMAI-$CsPbI_3$ annealed samples have been shown in Figure S14. Comparison of the data obtained on $CsPbI_3$ and DMAI-$CsPbI_3$ annealed thin films revealed clear structural differences. In the pure $CsPbI_3$ annealed thin film the six iodine neighbours were arranged in two slightly different but statistically distinguishable Pb-I_1 and Pb-I_2 shells (Table S3), with about 10% of them closer to Pb, at 3.08

Å away, and the others at 3.18 Å. On the contrary a single iodine neighbour shell was found around 3.14 Å fitting the data from DMAI-$CsPbI_3$ sample. This finding indicated that doping with DMAI promotes the undistorted PbI_6 octahedral arrangement (see Table S3). Although affected by a certain degree of uncertainty due to the weakness of the signal and the necessary approximations, the analysis of the next neighbour shell provided further valuable information. The analysis individuated the 5 Cs atoms shell at 5.11 Å in $CsPbI_3$, accordingly to the γ-phase structure, while 8 iodine neighbours were found around 5.16 Å in DMAI-$CsPbI_3$ sample, accordingly to a cubic lattice symmetry, with only minor changes upon annealing.

These findings clearly indicate a higher-symmetry γ* phase for DMAI-$CsPbI_3$ at RT, consistent with the GIWAXS results, which revealed a highly symmetric crystal structure (γ*) at RT after cooling from 200°C. Through combined GIWAXS and XAFS analysis, we established a well-defined thermal-phase relationship between these two materials (see Figure 2D), highlighting their key differences. This understanding holds significant potential for guiding future research efforts.

Stabilization mechanisms: local strain and octahedral bond angle (Pb-I-Pb).

Annealing of DMAI-$CsPbI_3$ films at 200 °C for 1 minute yielded optimal stabilization of the black perovskite phase. Two potential contributors to this enhanced stability were initially identified: residual DMAI and the presence of approximately 5% Cs_4PbI_6 as a secondary phase. To elucidate the influence of residual DMAI on phase stability, a systematic stability study was conducted under ambient conditions (relative humidity ~60%) using samples annealed at 200 °C for varying durations: 0.25, 0.50, 0.75, and 1.0 minute. These annealing intervals were chosen to produce films with progressively decreasing levels of residual DMAI. Among the tested conditions, the film annealed for 1.0 minute exhibited the highest stability over time, as shown in Figure S15. In addition, two identical thin-film samples from the same batch were annealed at 200 °C for dwell times of 0.25 minute and 1 minute, respectively, and stored under identical dry box conditions for over a year. The sample with the 0.25-minute dwell time degraded within 2 months, while the 1-minute annealed sample remained stable for over 16 months. Therefore, these findings strongly indicate that the presence of residual DMAI is not responsible for the long-term stabilization of the black phase in DMAI-$CsPbI_3$ films. To further investigate the role of Cs_4PbI_6, we synthesized a control film consisting of $CsPbI_3$ with an intentionally introduced Cs_4PbI_6 phase, but without the addition of DMAI (see Materials and Methods section for synthesis) and checked the stability of the black phase with the Cs_4PbI_6 phase fraction (see Figure S16). The stability of this film was then compared to DMAI-$CsPbI_3$ films annealed at different temperatures to achieve a similar Cs_4PbI_6 phase fraction (see Figure S17 and S18). The comparison revealed that while Cs_4PbI_6 contributes to enhanced short-term stability (within 1–2 hours) (See Figure S16C), it does not account for the prolonged black-phase stability observed in the DMAI-$CsPbI_3$ system, which persists for several days (See Figure S18C). These findings indicate that the dominant stabilizing mechanism is not the Cs_4PbI_6 phase but rather the partial substitution of Cs^+ by DMA^+. This substitution is believed to induce local lattice strain, which plays an important role in enhancing the long-term structural stability of the black perovskite phase, as discussed in the following section.

After ruling out the effects of residual DMAI and the presence of Cs_4PbI_6, two pivotal factors emerge as key contributors to phase stability: spontaneous strain and octahedral tilting[9,40]. In this context, we calculated the orthorhombic spontaneous strain, denoted as ε_{orth}, derived from the formula $\varepsilon_{orth} = (\varepsilon_2 - \varepsilon_1)$, where $\varepsilon_2 = (b - a_0)/a_0$ and $\varepsilon_1 = (a - a_0)/a_0$. Here, ‘a’ and ‘b’ represent the normalized lattice parameters, while ‘a_0’ estimated by taking the cube root of the normalized unit cell volume[9]. These calculations were performed for three distinct scenarios: (i) the γ-phase of $CsPbI_3$ obtained after cooling from 350 °C, (ii) the γ-phase of DMAI-$CsPbI_3$ obtained after cooling from 350 °C, and (iii) the γ-phase of DMAI-$CsPbI_3$ obtained after cooling from 200 °C. Notably, both samples cooled from 350 °C exhibited similar spontaneous strain values. However, a significant difference was observed between $CsPbI_3$ cooled from 350 °C and DMAI-$CsPbI_3$ cooled from 200 °C, with the latter showing nearly a 50% reduction in ε_{orth} relative to $CsPbI_3$ cooled from 350 °C (Figure 3A). This substantial reduction provided compelling evidence for the stabilization mechanism facilitated by DMAI incorporation. The picture further crystallized through our analysis *via* Rietveld refinement, which revealed intriguing variations in the Pb-I-Pb octahedral bond angle (ϕ) for the third case as compared to the other two, as shown in Figure 3B. The significant increase in the octahedral bond angle for DMAI-$CsPbI_3$ cooled from 200 °C, compared to $CsPbI_3$ cooled from 350 °C (see Figure 3B), aligned with and substantiated the stabilization mechanism underlying the formation of the higher-symmetry lack phase of DMAI-$CsPbI_3$ observed after cooling from 200 °C.

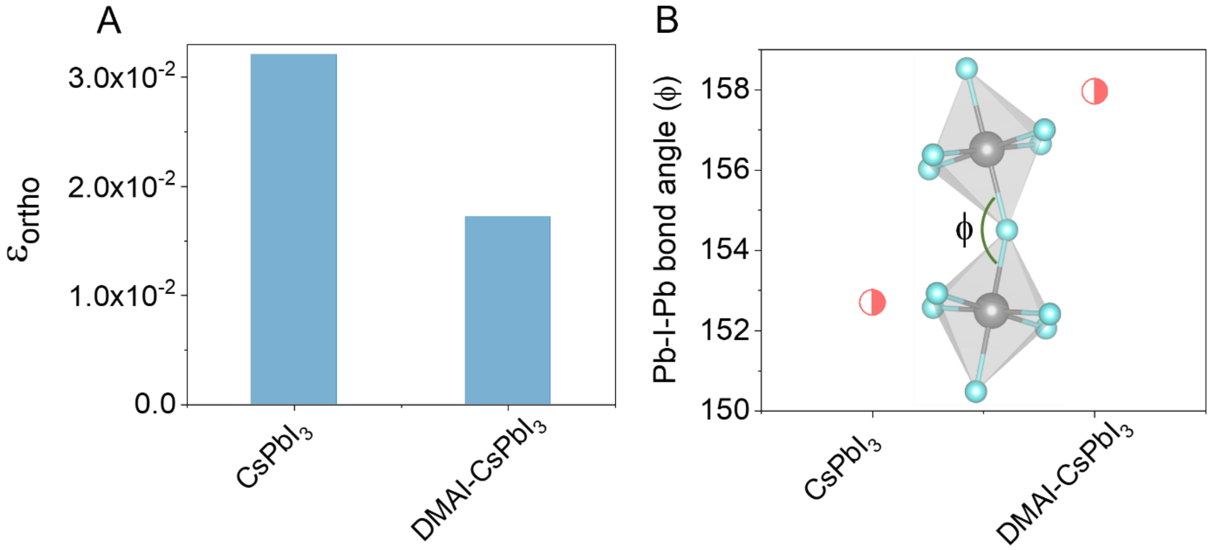

Figure 3. (A) Orthorhombic spontaneous strain (ε_{ortho}) at RT for $CsPbI_3$ (cooled from 350 °C) and DMAI-$CsPbI_3$ (cooled from 200 °C). (B) Average Pb-I-Pb octahedral bond angle (ϕ) for the RT black phase of $CsPbI_3$ (cooled from 350 °C) and DMAI-$CsPbI_3$ (cooled from 200 °C).

Tracing DMAI presence throughout the heat treatment.

To understand the role of DMAI in the crystallization process, it was essential to assess its presence in the system during heat treatment. This evaluation was examined through Thermogravimetric Analysis (TGA), and the results have been illustrated in Figure 4A-B. TGA data of $CsPbI_3$ revealed that dimethyl sulfoxide (DMSO) is fully evaporated at 120 °C, with no further weight loss observed beyond this temperature (See Figure 4A). In contrast, for DMAI-

$CsPbI_3$, a continuous mass loss is observed above 120 °C, extending up to 340 °C (See Figure 4B). The cooling data from 200 °C clearly affirm that a significant amount of DMAI is retained in the system, with the retention amount dependent on the dwelling time at 200 °C (See Figure 4B).

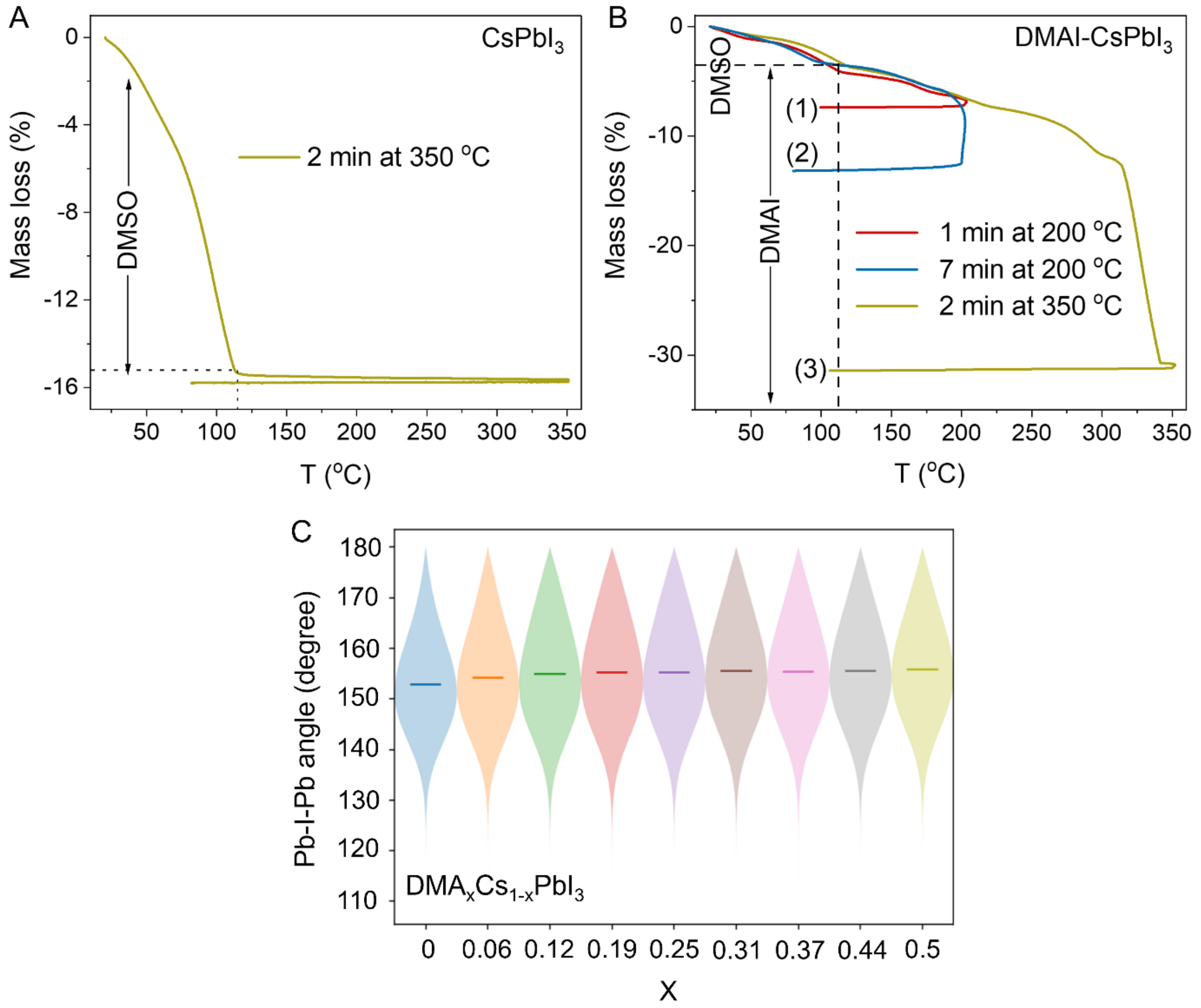

Figure 4. (A) Thermogravimetric analysis (TGA) of $CsPbI_3$ showing mass loss measured during heating and cooling cycles under an inert atmosphere. The $CsPbI_3$ sample was dried for a few hours to retain a significant amount of DMSO solvent, allowing for clear observation of mass loss during the heating cycle. (B) TGA of DMAI-$CsPbI_3$ showing mass loss during heating and cooling cycles under an inert atmosphere. The DMAI-$CsPbI_3$ sample was dried overnight to focus on DMAI evaporation. For DMAI-$CsPbI_3$, we employed different annealing strategies: (1) annealing up to 200 °C with a 1-minute dwell time before cooling, (2) annealing up to 200 °C with a 7-minute dwell time before cooling, and (3) annealing at 350 °C for 2 minutes before cooling. (C) Simulated Pb-I-Pb octahedral bond angles distribution of $DMA_xCs_{1-x}PbI_3$ with varying x.

In order to investigate the spatial distribution and incorporation of DMA^+ within the perovskite lattice, we performed a combination of complementary characterization techniques, namely synchrotron based HAXPES (Hard X ray Photoelectron Spectroscopy) and GIWAXS. These measurements were conducted on three types of samples: (i) DMAI-$CsPbI_3$ annealed at 200 °C, (ii) DMAI-$CsPbI_3$ annealed at 350 °C, and (iii) pure $CsPbI_3$ annealed at 350 °C (as shown in Figure S19). To ensure the reliability and reproducibility of the results, we measured several random spots across each sample, all of which gave consistent results. Importantly, to avoid surface contamination (such as carbon from environment), all steps - synthesis, annealing, and sample transport for HAXPES measurement were performed under an inert environment. In the HAXPES measurements, only the DMAI-$CsPbI_3$ sample cooled from 200 °C exhibited C 1s and N 1s peaks, whereas these peaks were absent in both the DMAI-$CsPbI_3$ sample annealed at 350 °C and the pure $CsPbI_3$ sample (as shown Figure S19A). This clearly confirms the presence of C 1s and N 1s peaks originating from DMA^+ in the DMAI-$CsPbI_3$ sample cooled from 200 °C. The incorporation of DMA ions also caused notable changes in the spectra of Cs 3d, I 3d, and Pb 4d compared to other two samples cooled from 350 °C (see Figure S19B). However, HAXPES alone does not provide direct evidence for the substitution of Cs^+ by DMA^+. To further investigate this, we performed GIWAXS measurements on the three sample types (Figure S19C). The DMAI-$CsPbI_3$ sample cooled from 200 °C exhibited a noticeable shift in the perovskite Bragg peaks toward lower q or 2θ angles relative to the DMAI-$CsPbI_3$ sample cooled from 350 °C and the pure $CsPbI_3$ sample (as shown Figure S19C). This shift is a strong indicator that a larger cation in this case, DMA^+ (ionic radii: 2.72 Å) has replaced Cs^+ (ionic radii: 1.88 Å) within the perovskite lattice.

Furthermore, to quantify the amount of DMA^+ substituting Cs, we employed Rietveld analysis of GIWAXS data along with theoretical calculations. The GIWAXS analysis of RT black phase of DMAI-$CsPbI_3$ indicated ~12–15% Cs^+ vacancies, which could, in principle, lead to Pb^{2+} enrichment. To examine this, we considered a scenario where these vacancies are charge-compensated by 6–7.5% excess Pb^{2+}. Due to the smaller ionic radius of Pb^{2+} (1.19 Å) compared to Cs^+ (1.88 Å), this would reduce the average ionic radius, resulting in unit cell contraction and a shift of GIWAXS peaks to higher 2θ (or q). Contrarily, GIWAXS data show the opposite: peaks shift to lower 2θ in DMAI-$CsPbI_3$ cooled from 200 °C (see Figure S19C), indicating lattice expansion due to incorporation of the larger DMA^+ cation, replacing Cs^+. Furthermore, Pb L_3-edge XANES spectra for both $CsPbI_3$ and DMAI-$CsPbI_3$ films showed no significant changes in edge position or shape, confirming that Pb valence and coordination remain unaffected by DMAI doping (see Figure S13A). Additionally, we observed an increase in the average Pb-I-Pb octahedral bond angle from 152° in $CsPbI_3$ to 158° in DMAI-$CsPbI_3$. To determine the exact amount of substitution, we simulated the Pb-I-Pb octahedral bond angle by replacing Cs with DMA^+ ions (See Figure 4C and Materials and Methods section for the details of theoretical calculation). Our simulations indicated that around 12% substitution an average Pb-I-Pb octahedral bond angle was obtained, which was consistent with the angle obtained from the Rietveld analysis. Therefore, we can conclude that for DMAI-$CsPbI_3$, around 12-15% of DMAI acted as a substitution for Cs, while the remaining functions as an additive within the system.

Impact of DMAI on the morphological properties of thin Films.

Having elucidated the crystallographic phases at various temperatures, it became imperative to comprehend the consequential morphological changes in two distinct sample types: $CsPbI_3$ and DMAI-$CsPbI_3$. Therefore, we conducted scanning electron microscopy (SEM) imaging, as depicted in Figure S20. The figure strikingly revealed that subsequent to cooling from 350 °C, the morphology of both materials exhibits remarkable similarity (similar type of grain and pin hole). However, in the case of DMAI-$CsPbI_3$, cooling from 200 °C exhibits a discernibly distinct morphology characterized by smaller grain size and increased compactness compared to other conditions.

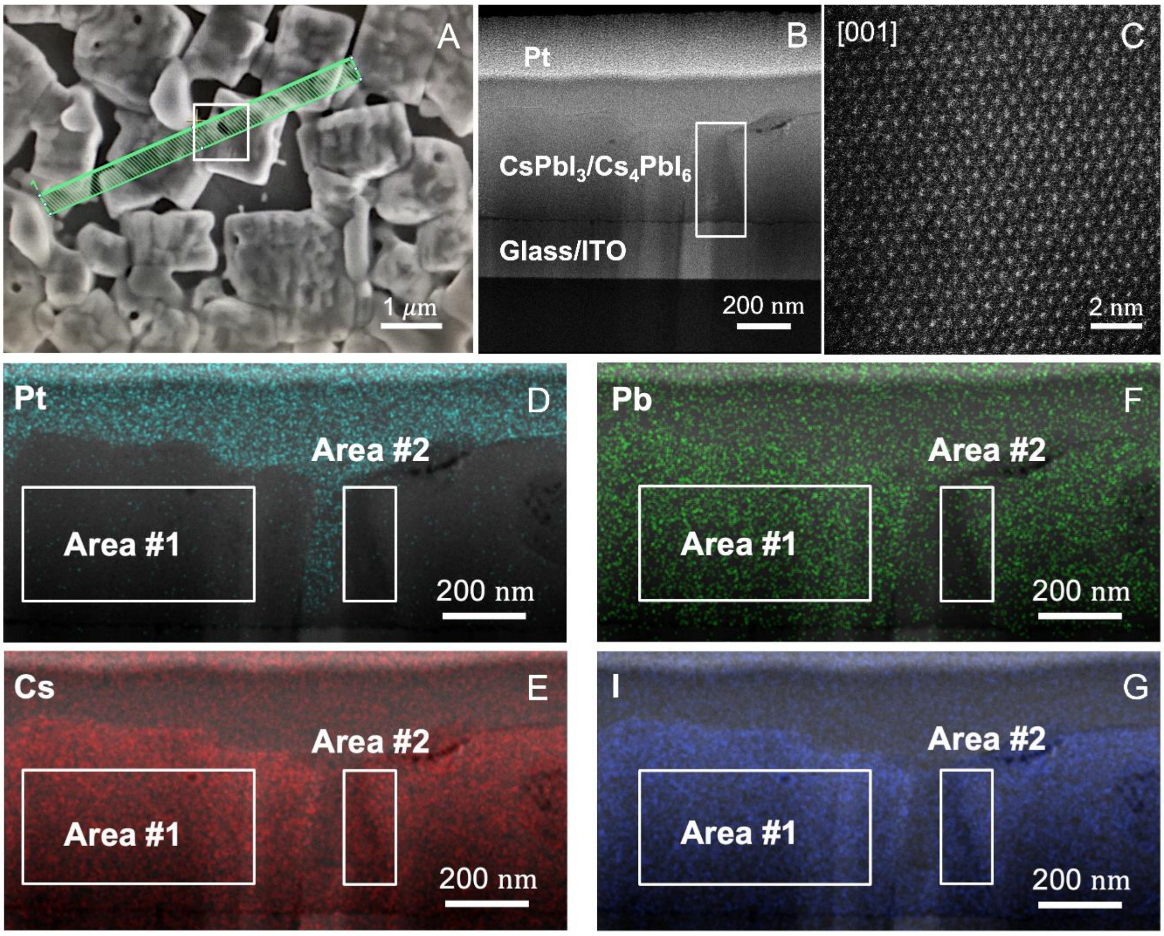

Figure 5. High-magnification SEM image of DMAI-CsPbI$_3$ film with assigned in green color region for FIB cutting (A). HAADF-STEM image (B) inside the white area of the FIB-prepared cross-section in (A). High resolution HAADF-STEM image (C) of a Cs$_4$PbI$_6$ region observed in the CsPbI$_3$ film (white box in (B)). Color-coded STEM-EDS elemental maps (D), (E), (F) and (G) for highlighted in white region in (A). Compositions calculated using the Cliff Lorimer method for area #1 are Cs 21.10±1.5 at.%, Pb 21.40±2.3 at.% and I 57.50±2.7 at.%, for area #2 - Cs 35.78±2.4 at.%, Pb 10.68±1.1 at.% and I 53.54±1.8 at.%.

However, for DMAI-CsPbI$_3$, pinholes were found in the grains (see Figure 5A). From the HAADF-STEM images of the FIB cross-section (Figure 5B), the thickness of the CsPbI$_3$ films was evaluated to be approximately 350 nm. The Z-contrast of the HAADF-STEM images (with intensity proportional to Z^2) enabled the detection of a low-contrast region near the pinhole of the film (indicated by the white frame in Figure 5B). Given that the perovskite layer contains a heavy element such as Pb, the lower contrast suggested the presence of a Pb-depleted phase. High-resolution HAADF-STEM images (Figure 5C) of this low-contrast region confirmed the presence of the Cs$_4$PbI$_6$ phase, belonging to the R-3c space group, as seen from the [001] orientation (Figure S21). Furthermore, STEM-EDS maps (Figure 5D-G) which include two areas *i.e*. area#1 in the perovskite $CsPbI_3$ and area#2 in Cs_4PbI_6 along with Cliff-Lorimer composition quantification, confirmed the expected stoichiometry. From the TEM study, we can confirm that in the case of DMAI-$CsPbI_3$, the pinholes are filled by the 0D Cs_4PbI_6 phase. This phase acts as a barrier, effectively preventing shunting during the fabrication of the device.

Translation of optimized thin films into photodetector devices.

We demonstrated that the incorporation of DMAI not only stabilized the black phase of $CsPbI_3$ but also improved the morphology of the thin film. However, the inclusion of DMAI within the $CsPbI_3$ crystal structure could potentially influence device performance. To evaluate the impact of the stabilized DMAI-$CsPbI_3$ thin film on device functionality, we fabricated photodetector devices and tested their performance under different applied reverse bias and acslight intensity. Prior to device fabrication, the bandgap of γ^*-DMAI-$CsPbI_3$ was assessed using UV-Vis absorption and photoluminescence (PL) spectroscopy (see Figure S22). These measurements revealed a slightly lower bandgap for DMAI-$CsPbI_3$ compared to $CsPbI_3$. This suggested that the stabilized phase retained its optical quality despite the structural modifications introduced by DMAI.

To determine the optimal efficiency, photodiodes were fabricated using two different DMAI-$CsPbI_3$ perovskite thin films, prepared with dwelling times of 1 minutes and 3 minutes at 200°C, following a stack configuration that adapted indium tin oxide (ITO) as the bottom electrode, nickel oxide (NiO_x) as the hole transport layer (HTL), titanium oxide (TiO_2) as the electron transport layer (ETL), and lastly aluminum (Al) as the top electrode. A schematic of the fabricated stack has been presented in Figure 6A. The 3-minute dwelling time (Figure S23) resulted in a higher dark current compared to 1 minutes (Figure 6B), confirming that the optimal efficiency was achieved with a 1-minute dwelling time.

Figure 6B showed the current density as a function of bias under various levels of incident light intensity for one of the champion fabricated devices. At -2 V, we obtained a dark current of 1.2×10^{-6} A/cm^2, which was comparable to what has been previously reported in literature for inorganic perovskite photodetectors[41–43]. At the same bias, the device's photocurrent response (J_{photon}) under 115 mW/cm^2 white illumination was 10.8 mA/cm^2, establishing a J_{photo} to J_{dark} ratio of ~9×10^3. As shown in Figure S24A, 8 out of 11 fabricated devices showed a J_{photo} to J_{dark} ratio between 2.5×10^3 and 1.2×10^4, placing confidence in the reliability of the reported device performance. In addition to low levels of dark current, high levels of EQE are desirable to ensure the efficient extraction of the photo-generated carriers. The device's EQE (shown in Figure 6C) reached a maximum of 77% at 430 nm at -2 V. Through the obtained EQE values, it is possible to calculate the specific detectivity (D*), a common figure of merit that describes the ability of a device to detect weak signals in the presence of noise. The device's specific detectivity at 430 nm (blue), 540 nm (green), and 630 nm (red) is equal to 4.3×10^{11} Jones, 5.0×10^{11} Jones, and 5.1×10^{11} Jones, respectively. Additionally, a photodetector's linear response to light intensity is a highly desirable feature for imaging applications. In this case, and as shown in Figure 6D, the photodetector has at least 100 dB of linear dynamic range at voltages between -2 and -0.5 V. Lastly, we measure the device's transient photocurrent response, presented in Figure S24B. The device yields a relatively fast response time under pulsed excitation, with the rise and fall time being in the range of 3 μs.

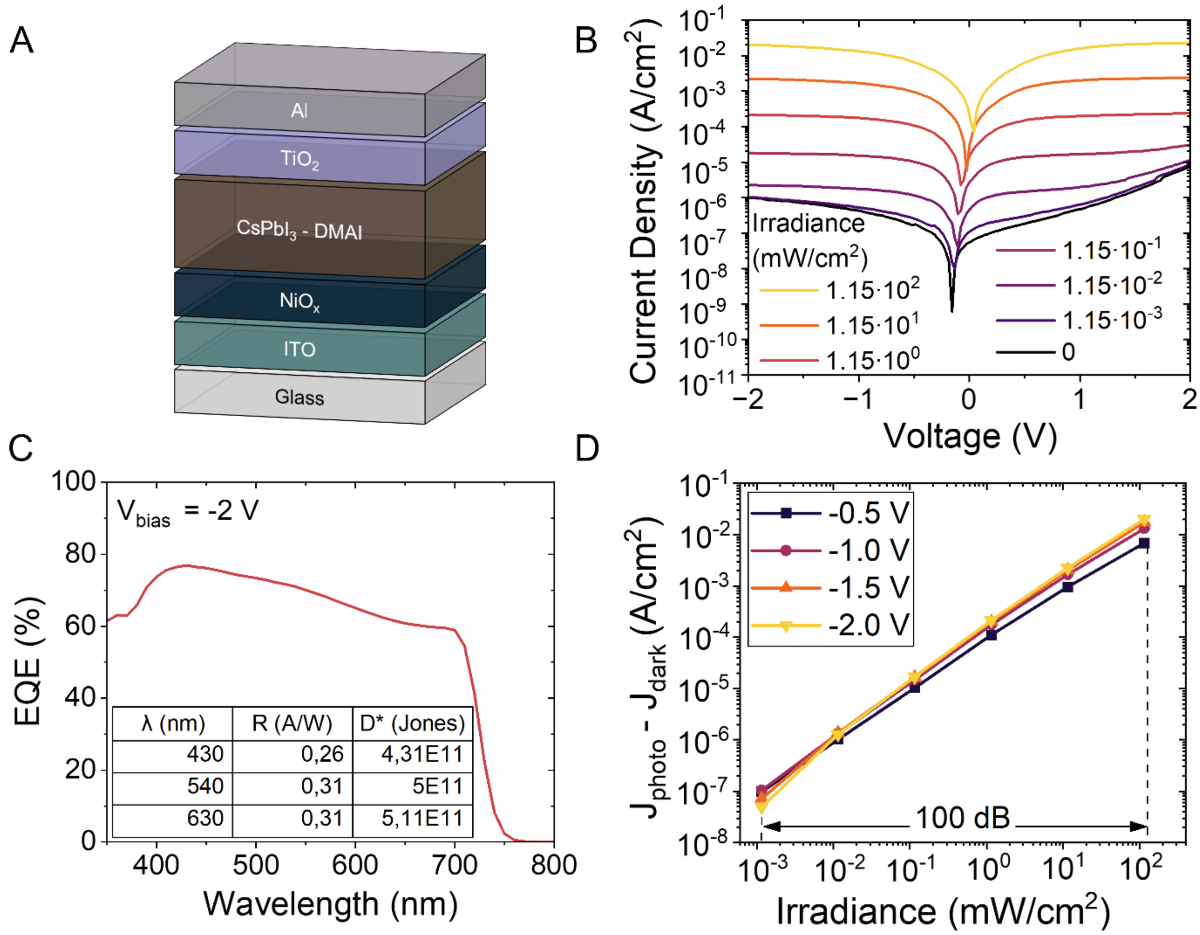

λ (nm)	R (A/W)	D* (Jones)
430	0,26	4,31E11
540	0,31	5E11
630	0,31	5,11E11

Figure 6. (A) Schematic structure of the DMAI-$CsPbI_3$ photodetector. (B) A DMAI-$CsPbI_3$ (annealed at 200°C for time 1 min) photodetector's current density as a function of bias in darkness and under the illumination of a white LED with various irradiances. (C) EQE as a function of wavelength under -2 V bias. The inset table reports the detector's responsivity and specific detectivity for various light wavelengths. (D) Linearity plot at -2.0 V, -1.5 V, -1 V, and -0.5 V, showing the difference between J_{photo} and J_{dark} as a function of light intensity.

Conclusion

In this study, we successfully enhanced the stability of the high-symmetry black phase of $CsPbI_3$ and improved thin-film morphology through controlled DMAI doping, while establishing a stabilization mechanism supported by experimental observations and theoretical calculations. Through a comprehensive investigation of structural, optical, and electronic properties, as well as photodetector device applications, we established the role of DMAI in stabilizing the black phase of $CsPbI_3$. By optimizing the amount of DMAI, annealing temperature, and dwelling time at 200 °C, we significantly extended the stabilization time of the black phase to up to seven days under ambient conditions (35–52% relative humidity) and remains stable for 16 months under dry box environment. Synchrotron-based GIWAXS and XAFS analyses revealed that the incorporation of DMA^+ during synthesis promoted the formation of a higher-symmetric black phase, intermediate between the γ- and β-phases, at room temperature. Rietveld refinement of GIWAXS data and theoretical simulations confirmed that 12–15% of DMA^+ replaces Cs^+ in the crystal structure, enhancing the Pb-I-Pb octahedral bond angle and reducing spontaneous orthorhombic strain., which stabilizes the black phase. The thin film morphology was also improved by the presence of 0D Cs_4PbI_6 phases, which filled pinholes in the films. We further validated the quality of the optimized thin films by fabricating photodetector devices and testing their performance under different reverse bias conditions and varying light intensities. These tests demonstrated the promising performance of DMAI-$CsPbI_3$ films, achieving 80% EQE and exhibiting a linear relationship between photocurrent and dark current differences across various irradiation levels, extending up to 100 dB. This study not only elucidates the stabilization mechanism of DMAI-$CsPbI_3$ but also identifies the optimal conditions for achieving superior stability and device functionality. Our findings pave the way for further advancements in photoconversion efficiency and provide insights for the development of high-performance solar cells and other optoelectronic applications.

Materials and Methods

Perovskite sample synthesis.

Without DMAI: The $CsPbI_3$ without dimethylammonium iodide (DMAI) sample was prepared by combining high-purity CsI (Aldrich, 99.9%) and PbI_2 (Aldrich, 99%) in stoichiometric ratio. Perovskite precursor solutions with concentrations of 0.8 mol/L were prepared in anhydrous dimethyl sulfoxide (DMSO), using the appropriate molar ratio of CsI and PbI_2 precursors to achieve the desired $CsPbI_3$ composition. The yellow perovskite precursor solutions were filtered through a 0.45 μm PTFE filter and then spin-coated onto glass substrates in a controlled environment within a nitrogen glove box. The spin-coating process was conducted at 4000 rpm for 60 seconds, ensuring a uniform film deposition. Subsequently, the thin films were annealed on a hotplate at 120 °C for 120 seconds to help evaporate remaining solvent, enhancing their crystallinity and structural integrity. Corresponding chemical reaction is: $CsI + PbI_2 \rightarrow CsPbI_3$.

With DMAI: The same synthesis procedure was applied for DMAI-$CsPbI_3$ as with the pure $CsPbI_3$. To assess the influence of DMAI, we employed three different ratios of DMAI:PbI_2:CsI, specifically 0.5:1:1, 1.2:1:1, and 1.5:1:1. We maintained a consistent precursor solution concentration and spin coater revolutions per minute (rpm) for comparison with the pure $CsPbI_3$ (without DMAI) thin film.

Optimization of the ratio of the precursors: To optimize the precursor ratio effectively, we have focused on the parameter "Stability of the black phase". The stability of the black phase under ambient conditions was monitored using stereo microscope imaging. For DMAI:PbI_2:CsI at ratios of 0.5:1:1, the complete conversion of the black phase to the yellow phase occurred within one hour (see Figure S1). Conversely, ratios of 1.2:1:1 and 1.5:1:1 exhibited similar stability, lasting 6-7 days. However, at a ratio of 2:1:1, more side phases (such as Cs_4PbI_6 with a band gap of approximately 3.38 eV[44]) were observed, diminishing the fraction of $CsPbI_3$ phase, which is undesirable for the intended application. Based on these findings, it is evident that the optimized ratio falls within the range of DMAI 1.2 to 1.5. For our investigations, we opt for DMAI 1.2 to prevent an excess of volatile organic cation.

Chemical reactions: In case of DMAI-$CsPbI_3$ synthesis, CsI, PbI_2, and DMAI were dissolved in DMSO to prepare a precursor solution containing Cs^+, Pb^{2+}, I^-, and DMA^+ ions. After spin-coating, the films were left to dry overnight inside a glovebox, allowing the most thermodynamically favorable phases to form. To monitor the phase evolution with temperature, *in situ* temperature-dependent GIWAXS measurements were performed (see Figure R25A). For quantitative analysis, Rietveld refinement was carried out on selected GIWAXS patterns at various temperatures (see Figure S25B). At room temperature, the GIWAXS data and corresponding refinement indicate that the film primarily consists of ~75% $DMAPbI_3$ and ~25% Cs_4PbI_6. This suggests that in the presence of Cs^+, Pb^{2+}, I^-, and DMA^+ ions, $DMAPbI_3$ forms preferentially due to its higher thermodynamic stability. The formation of $DMAPbI_3$ consumes a portion of the Pb^{2+}, leading to excess Cs^+, which subsequently drives the formation of the 0D Cs_4PbI_6 phase. Upon annealing at 200 °C, the phase composition shifts to ~95% $Cs_{0.85}DMA_{0.15}PbI_3$ and ~5% Cs_4PbI_6. This transition indicates that DMAI begins to evaporate with heating, causing $DMAPbI_3$ to decompose. The liberated Pb^{2+} restores the Cs^+/Pb^{2+} ratio toward $CsPbI_3$ stoichiometry, thus reducing Cs_4PbI_6 content. Finally, annealing at 350 °C results in complete evaporation of DMAI. GIWAXS analysis confirms the disappearance of Cs_4PbI_6 and the formation of pure $CsPbI_3$ with no signs of Cs-site vacancies.

These results clearly support the following reaction mechanism and demonstrate the phase evolution as a function of thermal annealing.

With DMAI case:

$1.2DMAI + CsI + PbI_2 \rightarrow 0.75DMAPbI_3 + 0.25Cs_4PbI_6 + 0.45DMAI\uparrow$ [RT]

$\rightarrow 0.95DMA_{0.15}Cs_{0.85}PbI_3 + 0.05Cs_4PbI_6 + 1.05DMAI\uparrow$ [200 °C]

$\rightarrow CsPbI_3 + 1.2DMAI\uparrow$ [above 200 °C]

$\rightarrow CsPbI_3$ [Cooling from 350 °C]

Formation of Cs_4PbI_6 phase with $CsPbI_3$ (without using DMAI): We synthesized mixed-phase films by varying the $CsI:PbI_2$ ratio without adding DMAI (see reaction below). By increasing the CsI content, we systematically induced the formation of Cs_4PbI_6, as confirmed by Rietveld refinement of synchrotron-based GIWAXS data (see Figure S16). The compositions and corresponding Cs_4PbI_6 content are as follows:

$CsI + PbI_2 \rightarrow CsPbI_3$ [0% Cs_4PbI_6]

$1.09\ CsI + PbI_2 \rightarrow 0.97\ CsPbI_3 + 0.03\ Cs_4PbI_6$ [3% Cs_4PbI_6]

$1.21\ CsI + PbI_2 \rightarrow 0.93\ CsPbI_3 + 0.07\ Cs_4PbI_6$ [7% Cs_4PbI_6]

$1.45\ CsI + PbI_2 \rightarrow 0.85\ CsPbI_3 + 0.15\ Cs_4PbI_6$ [15% Cs_4PbI_6]

Imaging using stereo microscopic. We conducted a comprehensive analysis of the stability of thin films at ambient condition shortly after thermal quenching under nitrogen using an advanced optical microscope (Leica DMS300). To further enhance our analysis, we utilized the powerful image processing capabilities of Image J software to discern and quantify the black-to-yellow color conversion from the image file captured by the Leica DMS300.

Thermogravimetric analysis (TGA). Thermogravimetric analysis (TGA) data were recorded using a TGA-Q500 instrument. The sample was weighed using a quartz balance, and heating was performed with a furnace, while cooling occurred through natural cooling. All measurements were conducted under a nitrogen (N_2) environment. For the $CsPbI_3$ sample prepared using DMSO solvent, we used partially dry $CsPbI_3$ powder to determine the temperature for complete evaporation, aiming to track the maximum weight loss due to DMSO, and annealed the sample up to 370°C. For DMAI-$CsPbI_3$, we employed different strategies: (1) annealing up to 200°C with a 1-minute dwell time before cooling, (2) annealing up to 200°C with a 7-minute dwell time before cooling, and (3) annealing at 350°C for 2 minutes before cooling.

Hard X-ray photoelectron spectroscopy (HAXPES). Hard X-ray photoelectron spectroscopy (HAXPES) measurements were conducted at BM25-SpLine beamline at the European Synchrotron Radiation Facility (ESRF) in Grenoble, France, using a photon energy of 11 keV. The samples were mounted within an ultra-high vacuum chamber to ensure optimal measurement conditions. The acquired data were analyzed using KOL XPD software, allowing for detailed examination of the electronic structure of the samples.

Scanning electron microscopy (SEM). The samples were subjected to SEM characterizations using the cutting-edge FEI Quanta FEG-250 scanning electron microscope. In order to mitigate any potential surface charging effects, a meticulously applied gold (60%)-palladium (40%) coating was deposited on the surface of the thin film. This coating served to facilitate optimal imaging conditions, enabling the acquisition of clear and detailed visualizations of the $CsPbI_3$ samples. Acceleration voltages of 5 or 15 kV were employed during the imaging process.

Transmission electron microscope (TEM). $CsPbI_3$ films on ITO/glass substrate were first imaged with FEI Helios Nanolab 650 scanning electron microscope (SEM). For further local analysis of the structure and composition with transmission electron microscope (TEM), cross-sections (70 nm thickness) of the film were prepared using focused ion beam (FIB). Prior to FIB cutting, Pt layer was deposited as protective layer. Prepared FIB lamellas were subjected to high angle annular dark field scanning transmission electron microscopy (HAADF-STEM) imaging. The images were acquired in a low-dose ($<1500\ e^-/Å^2$) regime using a probe-corrected Thermo FisherTitan Themis Z microscope operated at 300 kV with a probe semi-convergence angle of 21 mrad and equipped with a 4 quadrant Super X detector for energy dispersive x-ray spectroscopy (EDS). Acquisition time for EDS measurements was around 600 s.

Ultraviolet-visible (UV-vis) spectroscopy and photoluminescence (PL) spectroscopy. Diffuse reflectance measurements of the thin films were performed in a PerkinElmer Lambda 950 UV-Vis spectrophotometer. Emission spectra were captured employing the cutting-edge Edinburgh FLS980 fluorimeter, employing a 450 nm excitation source and corrected for the wavelength dependence of the detector channel.

Synchrotron-based Grazing Incidence Wide Angle X-ray Scattering (GIWAXS). Temperature-dependent GIWAXS (Grazing Incidence Wide Angle X-ray Scattering) data were recorded at the esteemed NCD-SWEET beamline, located at the ALBA synchrotron in Cerdanyola del Vallès, Spain. For data acquisition, a monochromatic X-ray beam with a wavelength (λ) of 0.9574 Å and dimensions of $80 \times 30\ \mu m^2$ (horizontal × vertical) was employed, utilizing a Si (111) channel cut monochromator. The scattered signal was precisely captured by a Rayonix LX255-HS area detector with a binning mode of 2×2. To accurately determine the reciprocal q-space and sample-to-detector distance, Cr_2O_3 was utilized as a calibrant. For full penetration of the X-ray beam through the layer, an incident angle (α_i) of 1° was deliberately chosen. Throughout the data acquisition process, a continuous flow of N_2, air, and dry air was maintained over the sample. To analyze the collected two-dimensional (2D) images, azimuthal integration was performed using PyFAI[45], a reliable software tool. Subsequently, the resulting unit cell models were refined using the La Bail and Rietveld refinement method implemented in Fullprof[46], a comprehensive analysis software. This rigorous approach ensured accurate and precise characterization of the studied materials through temperature-dependent GIWAXS measurements.

***In situ* X-ray absorption spectroscopy.** X-ray absorption spectroscopy (XAS) measurements (experiment No. MA5686) at the Pb L_3-edge (13.035 keV) were conducted at the BM23 beamline[47] of the European Synchrotron Radiation Facility (ESRF) in Grenoble, France, for both $CsPbI_3$ and DMAI-$CsPbI_3$ thin film samples. The XAS spectra were measured at RT in fluorescence geometry using a ionization chamber to measure the incident intensity and single element Si-drift (Hitachi Vortex) detector coupled to FalconX electronics allowing for high saturation limit (10^6 cps). The maximum total count rate on the detector was limited to have death time less than 5% to ensure count linearity across the absorption edge. The Pb-Lα fluorescence yield was electronically selected (MCA). The x-ray beam energy calibration has been checked measuring the absorption signal from a Pb reference foil. The XAS data on $CsPbI_3$ and DMAI-$CsPbI_3$ thin films were collected before (pristine) and after annealing respectively at 350°C and 200°C. Annealing cycles have been performed in-situ to avoid air exposure.

The XAFS data were treated following the standard procedures for background subtraction, normalization and extraction of the structural EXAFS signal. The near-edge (XANES) data were used to get information about the valence state and local coordination chemistry around Pb in thin films with and without DMAI, before and after thermal treatments.

The data in the extended (EXAFS) regions[48] were quantitatively analyzed to get information about the Pb-coordination shells in the thin films. The EXAFS analysis was conducted quantitatively by fitting the k-weighted ($k\chi_{exp}$) data to the model curve in the $k = 3 - 11$ Å^{-1} range for pristine and annealed samples, respectively. The model curve $\chi_{model} = \sum_i k\chi_i$ was calculated as a sum of partial contributions (χ_i) from the neighboring coordination calculated using the standard EXAFS model assuming Gaussian disorder[49].

$$k\chi_i = S_0^2 \frac{N_i}{R_i} A_i \sin(2kR_i + \phi_i)\, e^{-2k^2\sigma_i^2} e^{-\frac{2R_i}{\lambda}}$$

Here, N_i, R_i, and σ_i^2 are the parameters describing the average local atomic structure round the average absorber in i-th neighbour shells in the sample, namely the number of neighbours (multiplicity), average distance, and mean square relative displacement. After preliminary check, the S_0^2 parameter, which empirically takes into account the effects of many-body losses in the one-electro approximation, was fixed to 0.91 for all analyses. The photoelectron amplitude A_i, phase ϕ_i, and mean free path λ functions were calculated using the FEFF8.2 program[50]. An atomic cluster calculated using the crystallographic model was used to calculate the atomic potentials self-consistent Hedin-Lundqvist model and the relevant coordination shells around the Pb absorber.

Devices fabrication and characterization.

Device Fabrication: For device fabrication, 3×3 cm^2 glass substrates with prepatterned ITO strips, purchased from Colorado Concept Coatings LLC (15 Ω), were used. The substrates were cleaned in an ultrasonic bath by sequentially submerging them (for 5 min at 50°C) in Extran, water, acetone, and isopropanol. Followingly, 15 nm thick NiO_x films were deposited on top of the substrates by reactive sputtering of a metallic nickel target using O_2 plasma in a Nebula system from Angstrom Engineering Inc. The NiO_x-coated substrates were then annealed in open air at 300°C for 5 minutes, before being transferred to a glovebox. A perovskite layer was spin-coated on top of the substrates, following the recipe described above. Afterwards, the samples were transferred in a high-vacuum chamber (Angstrom Engineering Inc.) to deposit 45 nm of TiO_2 films *via* e-beam evaporation (~0.3Å/sec). The device stack was completed by depositing 100 nm of Al contacts (0.5 Å/sec) in the same vacuum chamber, using corresponding shadow masks.

Device Characterization: The current-voltage (in darkness and under illumination) and transient photocurrent measurements were obtained in nitrogen environment using a PAIOS all-in-one system by Fluxim. A white LED was used as the illumination source. Spectral response measurements were performed using an in-house built setup. A light beam generated by a 150 W halogen lamp (OSRAM HLX 64633) was coupled into a monochromator (MSH-300), giving coverage over the range of 350 – 800 nm. The signal from the photodetector was collected by a current pre-amplifier (SR570) and lock-in amplifier (SR830). A silicon photodiode with known responsivity was used for calibration. The samples were placed in hermetically sealed holder to avoid their exposure to the ambient environment during measurements.

The photodetector's responsivity was calculated through the EQE values, as described by equation:

$$R = \frac{e}{hc/\lambda} \times EQE \quad (A/W)$$

where e is the electron charge, h is Planck's constant, c is the speed of light, and λ is the incoming wavelength.

Considering that shot noise is the main contributor to noise current in the dark and that the contributions of Johnson and flick noise are insignificant, the photodetector's specific detectivity was calculated through the equation:

$$D^* = \frac{R}{(2eJ_{dark})^{\frac{1}{2}}} \left(\frac{cmHz^{\frac{1}{2}}}{W}\right)$$

where J_{dark} is the dark current density of the device.

Theoretical calculation. The bond angle distribution plot in Figure 3C of the manuscript was generated by tracking all Pb-I-Pb bond angles during molecular dynamics (MD) simulations. A periodic supercell containing 64 formula units of $CsPbI_3$ was simulated. 9 different DMA concentrations, uniformly distributed from 0% (pure $CsPbI_3$) to 50% (32 randomly selected Cs atoms replaced with DMA in a random orientation), were investigated. For each concentration, 10 MD simulations were performed in parallel. For each DMA-substituted structure, a unique set of Cs atoms was randomly replaced with DMA to mitigate any potential variances. NPT molecular dynamics (MD) simulations were performed with Yaff, employing a machine learning potential (MLP) generated *via* an equivariant deep neural network[51,52]. Each simulation ran for 100 ps with a timestep of 0.5 fs, preceded by a 5 ps equilibration period. Temperature was maintained at 300 K using a Langevin thermostat (time constant: 100 fs)[53], while pressure was controlled at 0.1 MPa using a Langevin barostat (time constant: 1 ps)[54]. For the MLP, the MACE[51] architecture was used to predict the energy and forces. To train the

MLP, an ab initio data set is necessary, which was obtained *via* an active learning loop that is implemented in the psiflow[55] software package. Psiflow circumvents the heavy computational cost of generating a large dataset with ab initio MD simulations. Psiflow starts with a small dataset to create an initial MLP, which is then used to perform short MD simulations to generate new structures. After the evaluation of the ab initio energy and forces of these structures, a new MLP is trained, and the procedure is repeated until the complete phase space is explored. The initial dataset contained 10 structures for each of the 9 doping concentrations. Cs is substituted with DMA *via* a Python script, which keeps the perovskite framework fixed. This leads to structures with high energy. Therefore, 100 ps NPT MD simulations were performed with the universal MACE-MP-0[56] MLP to relax the generated structures before starting the active learning loop. The final structures of the MD simulations were evaluated with CP2K[57] using the PBE-D3(BJ) exchange correlation (XC) functional[58,59]. The plane wave basis set had a cut-off energy of 800 Ry and a relative cut-off of 40 Ry. This plane wave basis set was combined with the TZVP-MOLOPT-PBE-GTH basis and GTH pseudopotentials applied to all atoms[60–62]. To train the MACE MLP, the cut-off radius was set to 7 Å. The other settings are provided in Table S4. The active learning loop contained 10 iterations, each iteration performed 90 NPT MD simulation of 500 fs at 600 K and 0.1 MPa. The final data set contained 891 and 99 training and validation structures, respectively. The root mean square errors for the validation set of the final MLP were 0.4 meV per atom and 24.7 meV/Å. The MLP trained for approximately 3 hours and 30 minutes. The Python scripts containing all the relevant information for both workflows, *i.e.*, the active learning loop to train the MLP and the MD simulations to generate the bond angle distribution plot, are available at https://doi.org/10.5281/zenodo.12687077[63]. Moreover, the Python script to generate the DMA-substituted $CsPbI_3$ supercells is also provided, along with the ab initio data set that was used to train and validate the final MLP.

Associated Content

Supporting Information. Photographs showing kinetic trends in perovskite thin film phase stability, complementary 2D and 1D XRD profiles with structural refinements, EXAFS data and analysis, XPS data and analysis, SEM and HAADF-STEM images, UV-vis and PL spectra with corresponding analysis, supporting photodetector device results, and a table of crystal structures, EXAFS parameters and MACE architecture settings.

Author Information

Corresponding Authors

Rafikul Ali Saha - cMACS, Department of Microbial and Molecular systems, KU Leuven, Celestijnenlaan 200F, Heverlee, 3001 Belgium

Email: rafikulali.saha@kuleuven.be

Maarten B. J. Roeffaers - cMACS, Department of Microbial and Molecular systems, KU Leuven, Celestijnenlaan 200F, Heverlee, 3001 Belgium

Email: maarten.roeffaers@kuleuven.be

Authors

Athina Papadopoulou - imec, Kapeldreef 75, 3001 Leuven, Belgium

Rocío Ariza - cMACS, Department of Microbial and Molecular systems, KU Leuven, Celestijnenlaan 200F, Heverlee, 3001 Belgium

Giedrius Degutis - cMACS, Department of Microbial and Molecular systems, KU Leuven, Celestijnenlaan 200F, Heverlee, 3001 Belgium; , and imec, Kapeldreef 75, 3001 Leuven, Belgium

Irina Skvortsova - Electron Microscopy for Materials Science(EMAT) and NANOlab Center of Excellence, University of Antwerp, B-2020 Antwerp, Belgium

Tom Braeckevelt - Center for Molecular Modeling (CMM),Ghent University, Technologiepark 46, 9052 Zwijnaarde, Belgium; and Department of Chemistry, KU Leuven, Celestijnenlaan 200F, Leuven 3001, Belgium

Francesco De Angelis - Department of Science, Roma Tre University, via Della Vasca Navale 84, 00146 Rome, Italy

Eduardo Solano - NCD-SWEET beamline, ALBA synchrotron light source, 08290, Cerdanyola del Vallès, Barcelona, Spain

João Pedro de Sousa Gouveia dos Anjos - imec, Kapeldreef 75, 3001 Leuven, Belgium; and i3N/CENIMAT, Department of Materials Science, Faculty of Science and Technology, Universidade NOVA de Lisboa and CEMOP/UNINOVA, Campus de Caparica, 2829-516 Caparica, Portugal

Maria Isabel Pintor Monroy - imec, Kapeldreef 75, 3001 Leuven, Belgium

Ilya Mongilyov – Polymer chemistry and materials, Department of Chemistry, KU Leuven, Celestijnenlaan 200F, Heverlee, 3001 Belgium

Bart Goderis - Polymer chemistry and materials, Department of Chemistry, KU Leuven, Celestijnenlaan 200F, Heverlee, 3001 Belgium

Juan Rubio-Zuazo - BM25-SpLine Beamline at the ESRF,71 Avenue des Martyrs, Grenoble, 38043, France; and Instituto de Ciencia de Materiales de Madrid-CSIC, Sor Juana Inés de la Cruz, 3, Cantoblanco, 28049 Madrid, Spain

Jan Genoe - imec, Kapeldreef 75, 3001 Leuven, Belgium; and Department of Electrical Engineering (ESAT), KU Leuven, Kasteelpark Arenberg 10, 3001 Leuven, Belgium

Carlo Meneghini - Department of Science, Roma Tre University, via Della Vasca Navale 84, 00146 Rome, Italy

Julian A. Steele - Australian Institute for Bioengineering and Nanotechnology (AIBN), The University of Queensland, Brisbane, QLD, 4072, Australia; and School of Mathematics and Physics, The University of Queensland, Brisbane, QLD, 4072, Australia

Sara Bals - Electron Microscopy for Materials Science(EMAT) and NANOlab Center of Excellence, University of Antwerp, B-2020 Antwerp, Belgium

Veronique Van Speybroeck - Center for Molecular Modeling (CMM), Ghent University, Technologiepark 46, 9052 Zwijnaarde, Belgium

Johan Hofkens - Department of Chemistry, KU Leuven, Celestijnenlaan 200F, Leuven 3001, Belgium; and Department of Molecular Spectroscopy, Max Planck Institute for Polymer Research, Mainz 55128, Germany

Notes

The authors declare no competing financial interest.

Acknowledgements: This work is supported by iBOF-21-085 PERsist and Internal Funds KU Leuven (C14/23/090). We also acknowledge the financial support from the Fund for Scientific Research Flanders (FWO) under Project number S004322N (GigaPixel), G0A5923N (SUSTRAINABLE). I.S. acknowledges SB-FWO project 1SHA024N for funding. V.V.S. furthermore acknowledge the Research Fund of Ghent University (BOF) for its financial support. The computational resources and services used in this work were provided by VSC (Flemish Supercomputer Center), funded by the Research Foundation─Flanders (FWO), and the Flemish Government. R.A.S, E.S. and J.A.S thank the staff of the BL11 NCD-SWEET beamline for their assistance in recording the synchrotron GIWAXS data. R.A.S, C.M, and F.A acknowledge dr. Cesare Atzori for his help during the XAFS measurement. We acknowledge to the ESRF for beamtime at BM23 and BM25. R.A. acknowledges financial support from Marie Skłodowska-Curie grant agreement No 101149132.

Reference:

(1) He, R.; Wang, W.; Yi, Z.; Lang, F.; Chen, C.; Luo, J.; Zhu, J.; Thiesbrummel, J.; Shah, S.; Wei, K.; Luo, Y.; Wang, C.; Lai, H.; Huang, H.; Zhou, J.; Zou, B.; Yin, X.; Ren, S.; Hao, X.; Wu, L.; Zhang, J.; Zhang, J.; Stolterfoht, M.; Fu, F.; Tang, W.; Zhao, D. Improving Interface Quality for 1-Cm2 All-Perovskite Tandem Solar Cells. *Nature* **2023**, *618* (7963), 80–86. https://doi.org/10.1038/s41586-023-05992-y.

(2) Quan, L. N.; Rand, B. P.; Friend, R. H.; Mhaisalkar, S. G.; Lee, T.-W.; Sargent, E. H. Perovskites for Next-Generation Optical Sources. *Chem. Rev.* **2019**, *119* (12), 7444–7477. https://doi.org/10.1021/acs.chemrev.9b00107.

(3) Wang, P.; Zhang, X.; Zhou, Y.; Jiang, Q.; Ye, Q.; Chu, Z.; Li, X.; Yang, X.; Yin, Z.; You, J. Solvent-Controlled Growth of Inorganic Perovskite Films in Dry Environment for Efficient and Stable Solar Cells. *Nat Commun* **2018**, *9* (1), 2225. https://doi.org/10.1038/s41467-018-04636-4.

(4) Iqbal, Z.; Félix, R.; Musiienko, A.; Thiesbrummel, J.; Köbler, H.; Gutierrez-Partida, E.; Gries, T. W.; Hüsam, E.; Saleh, A.; Wilks, R. G.; Zhang, J.; Stolterfoht, M.; Neher, D.; Albrecht, S.; Bär, M.; Abate, A.; Wang, Q. Unveiling the Potential of Ambient Air Annealing for Highly Efficient Inorganic $CsPbI_3$ Perovskite Solar Cells. *J. Am. Chem. Soc.* **2024**, *146* (7), 4642–4651. https://doi.org/10.1021/jacs.3c11711.

(5) Qin, Z.; Zhou, H.; Li, S.; Xiang, J.; Guan, Z.; Zhang, H.; Ma, X.; Zhang, M.; Wu, J.; Yang, H. $CsPbI_3$ Based All-Inorganic Perovskite Solar Cells: Further Performance Enhancement of the Electron Transport Layer-Free Structure from Device Simulation. *Advcd Theory and Sims* **2023**, *6* (8), 2200805. https://doi.org/10.1002/adts.202200805.

(6) Steele, J. A.; Jin, H.; Dovgaliuk, I.; Berger, R. F.; Braeckevelt, T.; Yuan, H.; Martin, C.; Solano, E.; Lejaeghere, K.; Rogge, S. M. J.; Notebaert, C.; Vandezande, W.; Janssen, K. P. F.; Goderis, B.; Debroye, E.; Wang, Y.-K.; Dong, Y.; Ma, D.; Saidaminov, M.; Tan, H.; Lu, Z.; Dyadkin, V.; Chernyshov, D.; Van Speybroeck, V.; Sargent, E. H.; Hofkens, J.; Roeffaers, M. B. J. Thermal Unequilibrium of Strained Black $CsPbI_3$ Thin Films. *Science* **2019**, *365* (6454), 679–684. https://doi.org/10.1126/science.aax3878.

(7) Yao, Z.; Zhao, W.; Liu, S. (Frank). Stability of the $CsPbI_3$ Perovskite: From Fundamentals to Improvements. *J. Mater. Chem. A* **2021**, *9* (18), 11124–11144. https://doi.org/10.1039/D1TA01252E.

(8) Steele, J. A.; Lai, M.; Zhang, Y.; Lin, Z.; Hofkens, J.; Roeffaers, M. B. J.; Yang, P. Phase Transitions and Anion Exchange in All-Inorganic Halide Perovskites. *Acc. Mater. Res.* **2020**, *1* (1), 3–15. https://doi.org/10.1021/accountsmr.0c00009.

(9) Steele, J. A.; Prakasam, V.; Huang, H.; Solano, E.; Chernyshov, D.; Hofkens, J.; Roeffaers, M. B. J. Trojans That Flip the Black Phase: Impurity-Driven Stabilization and Spontaneous Strain Suppression in γ-$CsPbI_3$ Perovskite. *J. Am. Chem. Soc.* **2021**, *143* (28), 10500–10508. https://doi.org/10.1021/jacs.1c05046.

(10) Huang, J.; Wang, H.; Chen, C.; Liu, S. (Frank). Enhancement of CsPbI3 Perovskite Solar Cells with Dual Functional Passivator 4-Fluoro-3-Phenoxybenzaldehyde. *Surfaces and Interfaces* **2022**, *35*, 102477. https://doi.org/10.1016/j.surfin.2022.102477.

(11) Huang, Y.; Yin, W.-J.; He, Y. Intrinsic Point Defects in Inorganic Cesium Lead Iodide Perovskite $CsPbI_3$. *J. Phys. Chem. C* **2018**, *122* (2), 1345–1350. https://doi.org/10.1021/acs.jpcc.7b10045.

(12) Jin, H.; Debroye, E.; Keshavarz, M.; Scheblykin, I. G.; Roeffaers, M. B. J.; Hofkens, J.; Steele, J. A. It's a Trap! On the Nature of Localised States and Charge Trapping in Lead Halide Perovskites. *Mater. Horiz.* **2020**, *7* (2), 397–410. https://doi.org/10.1039/C9MH00500E.

(13) Yang, W.; Li, J.; Chen, X.; Feng, Y.; Wu, C.; Gates, I. D.; Gao, Z.; Ding, X.; Yao, J.; Li, H. Exploring the Effects of Ionic Defects on the Stability of $CsPbI_3$ with a Deep Learning Potential. *ChemPhysChem* **2022**, *23* (7), e202100841. https://doi.org/10.1002/cphc.202100841.

(14) Trots, D. M.; Myagkota, S. V. High-Temperature Structural Evolution of Caesium and Rubidium Triiodoplumbates. *Journal of Physics and Chemistry of Solids* **2008**, *69* (10), 2520–2526. https://doi.org/10.1016/j.jpcs.2008.05.007.

(15) Ke, W.; Spanopoulos, I.; Stoumpos, C. C.; Kanatzidis, M. G. Myths and Reality of HPbI3 in Halide Perovskite Solar Cells. *Nat Commun* **2018**, *9* (1), 4785. https://doi.org/10.1038/s41467-018-07204-y.

(16) Bai, F.; Zhang, J.; Yuan, Y.; Liu, H.; Li, X.; Chueh, C.; Yan, H.; Zhu, Z.; Jen, A. K. -Y. A 0D/3D Heterostructured All-Inorganic Halide Perovskite Solar Cell with High Performance and Enhanced Phase Stability. *Advanced Materials* **2019**, *31* (48), 1904735. https://doi.org/10.1002/adma.201904735.

(17) Saha, R. A.; Chiu, W.-H.; Degutis, G.; Chen, P.; Filez, M.; Solano, E.; Orlov, N.; De Angelis, F.; Ariza, R.; Meneghini, C.; Detavernier, C.; Mali, S. S.; Hoang, M. T.; Yang, Y.; Garnett, E. C.; Wang, L.; Wang, H.; Roeffaers, M. B. J.; Steele, J. A. Oxygen-Mediated (0D) Cs_4PbX_6 Formation during Open-Air Thermal Processing Improves Inorganic Perovskite Solar Cell Performance. *ACS Nano* **2024**, *18* (26), 16994–17006. https://doi.org/10.1021/acsnano.4c03222.

(18) Kawano, Y.; Nakagawa, A.; Chantana, J.; Nishimura, T.; Mavlonov, A.; Minemoto, T. Impacts of 0D Cs4PbI6 Phase in All-Inorganic CsPbI3 Perovskites on Their Physical, Optical Properties and Photovoltaic Performances. *Thin Solid Films* **2022**, *759*, 139485. https://doi.org/10.1016/j.tsf.2022.139485.

(19) Tian, J.; Zhang, K.; Xie, Z.; Peng, Z.; Zhang, J.; Osvet, A.; Lüer, L.; Kirchartz, T.; Rau, U.; Li, N.; Brabec, C. J. Quantifying the Energy Losses in $CsPbI_2Br$ Perovskite Solar Cells with an Open-Circuit Voltage of up to 1.45 V. *ACS Energy Lett.* **2022**, *7* (11), 4071–4080. https://doi.org/10.1021/acsenergylett.2c01883.

(20) Liu, X.; Li, J.; Cui, X.; Wang, X.; Yang, D. The Progress and Efficiency of $CsPbI_2Br$ Perovskite Solar Cells. *J. Mater. Chem. C* **2023**, *11* (2), 426–455. https://doi.org/10.1039/D2TC03631B.

(21) Hu, Y.; Cai, L.; Xu, Z.; Wang, Z.; Zhou, Y.; Sun, G.; Sun, T.; Qi, Y.; Zhang, S.; Tang, Y. High-Efficiency $CsPbI_2Br$ Perovskite Solar Cells with over 83% Fill Factor by Synergistic Effects of a Multifunctional Additive. *Inorg. Chem.* **2023**, *62* (14), 5408–5414. https://doi.org/10.1021/acs.inorgchem.2c04316.

(22) Jeong, M. J.; Jeon, S. W.; Kim, S. Y.; Noh, J. H. High Fill Factor $CsPbI_2Br$ Perovskite Solar Cells Via Crystallization Management. *Advanced Energy Materials* **2023**, *13* (23), 2300698. https://doi.org/10.1002/aenm.202300698.

(23) Bian, H.; Wang, H.; Li, Z.; Zhou, F.; Xu, Y.; Zhang, H.; Wang, Q.; Ding, L.; Liu, S. (Frank); Jin, Z. Unveiling the Effects of Hydrolysis-Derived DMAI/$DMAPbI_x$ Intermediate Compound on the Performance of $CsPbI_3$ Solar Cells. *Adv. Sci.* **2020**, *7* (9), 1902868. https://doi.org/10.1002/advs.201902868.

(24) Wang, Y.; Liu, X.; Zhang, T.; Wang, X.; Kan, M.; Shi, J.; Zhao, Y. The Role of Dimethylammonium Iodide in $CsPbI_3$ Perovskite Fabrication: Additive or Dopant? *Angew. Chem. Int. Ed.* **2019**, *58* (46), 16691–16696. https://doi.org/10.1002/anie.201910800.

(25) Eperon, G. E.; Stone, K. H.; Mundt, L. E.; Schloemer, T. H.; Habisreutinger, S. N.; Dunfield, S. P.; Schelhas, L. T.; Berry, J. J.; Moore, D. T. The Role of Dimethylammonium in Bandgap

Modulation for Stable Halide Perovskites. *ACS Energy Lett.* **2020**, *5* (6), 1856–1864. https://doi.org/10.1021/acsenergylett.0c00872.

(26) Meng, H.; Shao, Z.; Wang, L.; Li, Z.; Liu, R.; Fan, Y.; Cui, G.; Pang, S. Chemical Composition and Phase Evolution in DMAI-Derived Inorganic Perovskite Solar Cells. *ACS Energy Lett.* **2020**, *5* (1), 263–270. https://doi.org/10.1021/acsenergylett.9b02272.

(27) Liu, C.; Sun, X.; Yang, Y.; Syzgantseva, O. A.; Syzgantseva, M. A.; Ding, B.; Shibayama, N.; Kanda, H.; Fadaei Tirani, F.; Scopelliti, R.; Zhang, S.; Brooks, K. G.; Dai, S.; Cui, G.; Irwin, M. D.; Shao, Z.; Ding, Y.; Fei, Z.; Dyson, P. J.; Nazeeruddin, M. K. Retarding Solid-State Reactions Enable Efficient and Stable All-Inorganic Perovskite Solar Cells and Modules. *Sci. Adv.* **2023**, *9* (21), eadg0087. https://doi.org/10.1126/sciadv.adg0087.

(28) Sun, X.; Shao, Z.; Li, Z.; Liu, D.; Gao, C.; Chen, C.; Zhang, B.; Hao, L.; Zhao, Q.; Li, Y.; Wang, X.; Lu, Y.; Wang, X.; Cui, G.; Pang, S. Highly Efficient CsPbI3/Cs1-xDMAxPbI3 Bulk Heterojunction Perovskite Solar Cell. *Joule* **2022**, *6* (4), 850–860. https://doi.org/10.1016/j.joule.2022.02.004.

(29) Sun, X.; Shao, Z.; Rao, Y.; Meng, H.; Gao, C.; Chen, C.; Liu, D.; Lv, P.; Li, Z.; Wang, X.; Cui, G.; Pang, S. A Low-Temperature Additive-Involved Leaching Method for Highly Efficient Inorganic Perovskite Solar Cells. *Advanced Energy Materials* **2021**, *11* (1), 2002754. https://doi.org/10.1002/aenm.202002754.

(30) Tan, X.; Wang, S.; Zhang, Q.; Liu, H.; Li, W.; Zhu, L.; Chen, H. Stabilizing CsPbI3 Perovskite for Photovoltaic Applications. *Matter* **2023**, *6* (3), 691–727. https://doi.org/10.1016/j.matt.2022.12.012.

(31) Jin, H.; Zeng, Y.-J.; Steele, J. A.; Roeffaers, M. B. J.; Hofkens, J.; Debroye, E. Phase Stabilization of Cesium Lead Iodide Perovskites for Use in Efficient Optoelectronic Devices. *NPG Asia Mater* **2024**, *16* (1), 24. https://doi.org/10.1038/s41427-024-00540-0.

(32) Kim, J. Y.; Lee, J.-W.; Jung, H. S.; Shin, H.; Park, N.-G. High-Efficiency Perovskite Solar Cells. *Chem. Rev.* **2020**, *120* (15), 7867–7918. https://doi.org/10.1021/acs.chemrev.0c00107.

(33) Khatoon, S.; Kumar Yadav, S.; Chakravorty, V.; Singh, J.; Bahadur Singh, R.; Hasnain, M. S.; Hasnain, S. M. M. Perovskite Solar Cell's Efficiency, Stability and Scalability: A Review. *Materials Science for Energy Technologies* **2023**, *6*, 437–459. https://doi.org/10.1016/j.mset.2023.04.007.

(34) Roy, P.; Ghosh, A.; Barclay, F.; Khare, A.; Cuce, E. Perovskite Solar Cells: A Review of the Recent Advances. *Coatings* **2022**, *12* (8), 1089. https://doi.org/10.3390/coatings12081089.

(35) Wang, H.; Liu, H.; Dong, Z.; Li, W.; Zhu, L.; Chen, H. Composition Manipulation Boosts the Efficiency of Carbon-Based CsPbI3 Perovskite Solar Cells to beyond 14%. *Nano Energy* **2021**, *84*, 105881. https://doi.org/10.1016/j.nanoen.2021.105881.

(36) Khanna, Y. P.; Taylor, T. J. Comments and Recommendations on the Use of the Avrami Equation for Physico-chemical Kinetics. *Polymer Engineering & Sci* **1988**, *28* (16), 1042–1045. https://doi.org/10.1002/pen.760281605.

(37) Goldschmidt, V. M. Die Gesetze der Krystallochemie. *Naturwissenschaften* **1926**, *14* (21), 477–485. https://doi.org/10.1007/bf01507527.

(38) Li, Z.; Yang, M.; Park, J.-S.; Wei, S.-H.; Berry, J. J.; Zhu, K. Stabilizing Perovskite Structures by Tuning Tolerance Factor: Formation of Formamidinium and Cesium Lead Iodide Solid-State Alloys. *Chem. Mater.* **2016**, *28* (1), 284–292. https://doi.org/10.1021/acs.chemmater.5b04107.

(39) *Synchrotron Radiation: Basics, Methods and Applications*; Mobilio, S., Boscherini, F., Meneghini, C., Eds.; Springer Berlin Heidelberg: Berlin, Heidelberg, 2015. https://doi.org/10.1007/978-3-642-55315-8.

(40) Carpenter, M. A.; Salje, E. K. H.; Graeme-Barber, A. Spontaneous Strain as a Determinant of Thermodynamic Properties for Phase Transitions in Minerals. *ejm* **1998**, *10* (4), 621–691. https://doi.org/10.1127/ejm/10/4/0621.

(41) Pintor Monroy, M. I.; Goldberg, I.; Elkhouly, K.; Georgitzikis, E.; Clinckemalie, L.; Croes, G.; Annavarapu, N.; Qiu, W.; Debroye, E.; Kuang, Y.; Roeffaers, M. B. J.; Hofkens, J.; Gehlhaar, R.; Genoe, J. All-Evaporated, All-Inorganic CsPbI $_3$ Perovskite-Based Devices for Broad-Band Photodetector and Solar Cell Applications. *ACS Appl. Electron. Mater.* **2021**, *3* (7), 3023–3033. https://doi.org/10.1021/acsaelm.1c00252.

(42) Steele, J. A.; Braeckevelt, T.; Prakasam, V.; Degutis, G.; Yuan, H.; Jin, H.; Solano, E.; Puech, P.; Basak, S.; Pintor-Monroy, M. I.; Van Gorp, H.; Fleury, G.; Yang, R. X.; Lin, Z.; Huang, H.; Debroye, E.; Chernyshov, D.; Chen, B.; Wei, M.; Hou, Y.; Gehlhaar, R.; Genoe, J.; De Feyter, S.; Rogge, S. M. J.; Walsh, A.; Sargent, E. H.; Yang, P.; Hofkens, J.; Van Speybroeck, V.; Roeffaers, M. B. J. An Embedded Interfacial Network Stabilizes Inorganic CsPbI3 Perovskite Thin Films. *Nat Commun* **2022**, *13* (1), 7513. https://doi.org/10.1038/s41467-022-35255-9.

(43) Li, W.; Xu, Y.; Peng, J.; Li, R.; Song, J.; Huang, H.; Cui, L.; Lin, Q. Evaporated Perovskite Thick Junctions for X-Ray Detection. *ACS Appl. Mater. Interfaces* **2021**, *13* (2), 2971–2978. https://doi.org/10.1021/acsami.0c20973.

(44) Akkerman, Q. A.; Park, S.; Radicchi, E.; Nunzi, F.; Mosconi, E.; De Angelis, F.; Brescia, R.; Rastogi, P.; Prato, M.; Manna, L. Nearly Monodisperse Insulator Cs_4PbX_6 (X = Cl, Br, I) Nanocrystals, Their Mixed Halide Compositions, and Their Transformation into $CsPbX_3$ Nanocrystals. *Nano Lett.* **2017**, *17* (3), 1924–1930. https://doi.org/10.1021/acs.nanolett.6b05262.

(45) Ashiotis, G.; Deschildre, A.; Nawaz, Z.; Wright, J. P.; Karkoulis, D.; Picca, F. E.; Kieffer, J. The Fast Azimuthal Integration Python Library: *pyFAI. J Appl Crystallogr* **2015**, *48* (2), 510–519. https://doi.org/10.1107/S1600576715004306.

(46) Rodríguez-Carvajal, J. Recent Advances in Magnetic Structure Determination by Neutron Powder Diffraction. *Physica B: Condensed Matter* **1993**, *192* (1–2), 55–69. https://doi.org/10.1016/0921-4526(93)90108-I.

(47) De Angelis, F.; Degutis, G.; Meneghini, C.; Noia, M.; Saha, R. A. Probing Local Structural Disorder and Its Stabilizing Effect in Doped CsPbI3 Perovskite Using in Situ XAFS, 2026. https://doi.org/10.15151/ESRF-ES-1192836278.

(48) Meneghini, C.; Bardelli, F.; Mobilio, S. ESTRA-FitEXA: A Software Package for EXAFS Data Analysis. *Nuclear Instruments and Methods in Physics Research Section B: Beam Interactions with Materials and Atoms* **2012**, *285*, 153–157. https://doi.org/10.1016/j.nimb.2012.05.027.

(49) Bunker, G. *Introduction to XAFS: A Practical Guide to X-Ray Absorption Fine Structure Spectroscopy*, 1st ed.; Cambridge University Press, 2010. https://doi.org/10.1017/CBO9780511809194.

(50) Rehr, J. J.; Albers, R. C. Theoretical Approaches to X-Ray Absorption Fine Structure. *Rev. Mod. Phys.* **2000**, *72* (3), 621–654. https://doi.org/10.1103/RevModPhys.72.621.

(51) Batatia, I.; Kovács, D. P.; Simm, G. N. C.; Ortner, C.; Csányi, G. MACE: Higher Order Equivariant Message Passing Neural Networks for Fast and Accurate Force Fields. arXiv January 26, 2023. http://arxiv.org/abs/2206.07697 (accessed 2024-08-12).

(52) Batzner, S.; Musaelian, A.; Sun, L.; Geiger, M.; Mailoa, J. P.; Kornbluth, M.; Molinari, N.; Smidt, T. E.; Kozinsky, B. E(3)-Equivariant Graph Neural Networks for Data-Efficient and Accurate Interatomic Potentials. *Nat Commun* **2022**, *13* (1), 2453. https://doi.org/10.1038/s41467-022-29939-5.

(53) Bussi, G.; Parrinello, M. Accurate Sampling Using Langevin Dynamics. *Phys. Rev. E* **2007**, *75* (5), 056707. https://doi.org/10.1103/PhysRevE.75.056707.

(54) Feller, S. E.; Zhang, Y.; Pastor, R. W.; Brooks, B. R. Constant Pressure Molecular Dynamics Simulation: The Langevin Piston Method. *The Journal of Chemical Physics* **1995**, *103* (11), 4613–4621. https://doi.org/10.1063/1.470648.

(55) Vandenhaute, S.; Cools-Ceuppens, M.; DeKeyser, S.; Verstraelen, T.; Van Speybroeck, V. Machine Learning Potentials for Metal-Organic Frameworks Using an Incremental Learning Approach. *npj Comput Mater* **2023**, *9* (1), 19. https://doi.org/10.1038/s41524-023-00969-x.

(56) Batatia, I.; Benner, P.; Chiang, Y.; Elena, A. M.; Kovács, D. P.; Riebesell, J.; Advincula, X. R.; Asta, M.; Avaylon, M.; Baldwin, W. J.; Berger, F.; Bernstein, N.; Bhowmik, A.; Blau, S. M.; Cărare, V.; Darby, J. P.; De, S.; Della Pia, F.; Deringer, V. L.; Elijošius, R.; El-Machachi, Z.; Falcioni, F.; Fako, E.; Ferrari, A. C.; Genreith-Schriever, A.; George, J.; Goodall, R. E. A.; Grey, C. P.; Grigorev, P.; Han, S.; Handley, W.; Heenen, H. H.; Hermansson, K.; Holm, C.; Jaafar, J.; Hofmann, S.; Jakob, K. S.; Jung, H.; Kapil, V.; Kaplan, A. D.; Karimitari, N.; Kermode, J. R.; Kroupa, N.; Kullgren, J.; Kuner, M. C.; Kuryla, D.; Liepuoniute, G.; Margraf, J. T.; Magdău, I.-B.; Michaelides, A.; Moore, J. H.; Naik, A. A.; Niblett, S. P.; Norwood, S. W.; O'Neill, N.; Ortner, C.; Persson, K. A.; Reuter, K.; Rosen, A. S.; Schaaf, L. L.; Schran, C.; Shi,

B. X.; Sivonxay, E.; Stenczel, T. K.; Svahn, V.; Sutton, C.; Swinburne, T. D.; Tilly, J.; van der Oord, C.; Varga-Umbrich, E.; Vegge, T.; Vondrák, M.; Wang, Y.; Witt, W. C.; Zills, F.; Csányi, G. A Foundation Model for Atomistic Materials Chemistry. arXiv March 1, 2024. http://arxiv.org/abs/2401.00096 (accessed 2024-08-12).

(57) Hutter, J.; Iannuzzi, M.; Schiffmann, F.; VandeVondele, J. CP2K: Atomistic Simulations of Condensed Matter Systems. *WIREs Comput Mol Sci* **2014**, *4* (1), 15–25. https://doi.org/10.1002/wcms.1159.

(58) Perdew, J. P.; Burke, K.; Ernzerhof, M. Generalized Gradient Approximation Made Simple. *Phys. Rev. Lett.* **1996**, *77* (18), 3865–3868. https://doi.org/10.1103/PhysRevLett.77.3865.

(59) Grimme, S.; Antony, J.; Ehrlich, S.; Krieg, H. A Consistent and Accurate *Ab Initio* Parametrization of Density Functional Dispersion Correction (DFT-D) for the 94 Elements H-Pu. *The Journal of Chemical Physics* **2010**, *132* (15), 154104. https://doi.org/10.1063/1.3382344.

(60) Lippert, G.; Hutter, J.; Parrinello, M. A Hybrid Gaussian and Plane Wave Density Functional Scheme. *Mol. Phys.* **1997**, *92* (3), 477–487. https://doi.org/10.1080/002689797709482119.

(61) Goedecker, S.; Teter, M.; Hutter, J. Separable Dual-Space Gaussian Pseudopotentials. *Phys. Rev. B* **1996**, *54* (3), 1703–1710. https://doi.org/10.1103/PhysRevB.54.1703.

(62) VandeVondele, J.; Hutter, J. Gaussian Basis Sets for Accurate Calculations on Molecular Systems in Gas and Condensed Phases. *The Journal of Chemical Physics* **2007**, *127* (11), 114105. https://doi.org/10.1063/1.2770708.

(63) Tom Braeckevelt. Tbraeckevelt/cspbi3_substituted_DMA: V1.1, 2024. https://doi.org/10.5281/ZENODO.12687077.

TOC Graphic: Incorporation of DMAI stabilizes the higher-symmetry perovskite phase at room temperature by modulating the octahedral bonding arrangement and spontaneous orthorhombic strain.